Academy of Sciences of the Czech Republic

Abstract of the doctor of science thesis for the award of the scientific degree "doctor of science" in the category of sciences:
GEOPHYSICO / GEOLOGICAL SCIENCES (EARTH SCIENCES)

Thesis Title:

GRAVIMETRIC METHODS FOR MODELING THE LITHOSPHERIC STRUCTURES AND PROCESSES

Commission for Defending the Doctor of Science Degree in the field of science: **Geophysical Sciences**

Name and surname of the Candidate: **Robert Tenzer**

Candidate´s Place of Employment: **University of West Bohemia**

Place and Date: **Plzen, 20th of December, 2015**

Preface

Theoretical models and numerical studies for geophysical interpretations of the Earth's gravity field described here were formulated and compiled during my research stay in the Department of Remote Sensing and Geosciences at the Technical University in Delft (The Netherlands), and further developed during my lecturing in the National School of Surveying at the University of Otago (New Zealand) and the School of Geodesy and Geomatics at the Wuhan University (P.R. China). Theoretical definitions presented here were discussed with Prof. Lars E. Sjöberg (Royal Institute of Technology), Prof. Mohammad Bagherbandi (IT and Land Management University of Gävle), Prof. Mehdi Eshagh (University West), Prof. Pavel Novák (University of West Bohemia), and Dr. Peter Vajda (Slovak Academy of Sciences). The numerical studies were conducted with the help of Wenjin Shen (Wuhan University), Hamayun (Technical University in Delft), and Dr. Vladislav Gladkikh (University of Otago).

Resume

The research presented here describes methods for the gravimetric interpretation of the lithospheric density structure, and particularly the gravimetric determination of the crust-mantle (Moho) density interface. Moreover, methods for the gravimetric interpretation of geodynamic phenomena related with the mantle convection are presented, namely investigating the signature of the ocean-floor spreading and the sub-crustal stress in the gravity field. Focusing on global applications, all functional models are defined in the spectral domain. These functional models utilize methods for a spherical harmonic analysis and synthesis of the gravitational field and the lithospheric density structure. The practical applications of these methods are demonstrated in numerical studies for computing the Earth's spherical crustal density model, the gravimetric forward modeling of major known crustal density structures, compilation of the synthetic gravitational model of the oceanic lithosphere, solving the gravimetric inverse problem for finding the Moho depth, and the determination of the sub-crustal stress field.

After a brief introduction into the topic in Chapter 1, the fundamental definitions of the gravity field quantities are recapitulated in Chapter 2. In theoretical definitions, the spectral representation of a 3-D density distribution of volumetric mass layers is defined in Chapter 3. In practical examples, theoretical density models of the seawater and marine sediments are established based on analysis of available density samples in Chapter 4. The functional definitions describing a mass density distribution (in Chapter 3) are facilitated to compile the Earth's spectral crustal model (ESCM180) based on applying methods for a spherical harmonic analysis of the crustal density structures in Chapter 5. This functional density distribution model is further facilitated in deriving the spectral expressions for the gravimetric forward modeling in Chapter 6. The expressions for the gravimetric forward modeling are then applied to compute the gravitational contributions of major known crustal density structures based on applying methods for a spherical harmonic synthesis of the Earth's crustal structures. The applied methods and numerical results are discussed and presented in Chapter 7. The methods for the gravimetric forward modeling (Chapter 6) and theoretical density models

(Chapter 4) are also used to compile the synthetic gravitational model of the oceanic lithosphere in Chapter 8. This synthetic model describes the gravitational signature of a thermal state of the oceanic lithosphere as a function of the ocean-floor spreading (reflecting the density increase with age of the oceanic lithosphere) and the oceanic deepening (caused by a thermal contraction of the oceanic lithosphere). The spectral expressions for solving the gravimetric inverse problem for finding the Moho depth are provided in Chapter 9, and applied for a global Moho recovery in Chapter 10. The *a priori* models of the Earth's lithospheric structure and the Moho depth applied in these numerical studies were obtained from analysis of seismic results. In this way, the applied processing strategies combine the gravity and seismic models. The method of computing the horizontal components of the sub-crustal stress field is presented in Chapter 11. This method combines the Runcorn's solution to the Navier-Stokes' problem with the Vening Meinesz-Moritz's (VMM) inverse problem of isostasy for a simultaneous determination of the sub-crustal stress and the Moho depth. The distribution of the terrestrial sub-crustal stress field and its relation with tectonism is investigated in Chapter 12, and a similar study is conducted to investigate the stress pattern on Mars in Chapter 13. It is demonstrated that the spatial distribution of the sub-crustal stress on the Earth closely resembles global tectonic configuration, with maximum stress intensity induced by the mantle convection along active convergent tectonic margins. The Martian sub-crustal stress is, on the other hand, mainly attributed to the crustal loading and the regional tectonism associated with a volcanic evolution on Mars.

Table of Contents

1. INTRODUCTION

Seismic data represent the primary source of information used in studies of the Earth's inner density structure. However, large parts of the Earth are not yet sufficiently covered by seismic surveys. In areas where seismic data are sparse or completely missing, gravity measurements can be used. With the advent of three dedicated satellite-gravity missions, namely the Challenging Mini-satellite Payload (CHAMP), the Gravity Recovery and Climate Experiment (GRACE), and the Gravity field and steady-state Ocean Circulation Explorer (GOCE), the external gravitational field of the Earth has being observed with a high resolution and accuracy. The latest global gravitational models derived from these satellite missions have a spatial resolution about 80 km (in terms of a half-wavelength). Moreover, these gravitational models have (almost) global and homogeneous coverage, with well-defined stochastic properties. Further improvement by means of the resolution and accuracy of these models has been achieved by combining the satellite-gravity data with the ground-based, air-borne, and sea-borne gravity measurements over certain parts of the world where these gravity measurements are available, while the satellite-altimetry data improved the gravitational information over the oceans.

This improved information on the Earth's gravitational field was facilitated in numerous studies investigating the Earth's interior, focusing mainly on the crust and upper-mantle density composition, and including also studies of the Moho density interface and the structure of large sedimentary basins. Moreover, this information has been used for a better understanding of various geodynamic processes based on analysis of the temporal gravity variations as well as the spatial pattern of static gravity field. Whereas the long-wavelength spectrum of the Earth's gravitational field comprises mainly the signature of deep mantle density heterogeneities, the medium-to-higher frequency gravitational spectrum reflects the density composition of more shallow sources within the lithosphere. This allows studying and interpreting the gravitational features which are related, for instance, to the mantle convection, the global tectonism (such as the oceanic subduction, orogenic formations, earthquake mechanisms, and lithospheric plate configuration), the lithospheric stress field, the isostatic compensation mechanisms, the glacial isostatic adjustment, and other related geodynamic phenomena. Since

the gravity observations could not solely be used to interpret the Earth's inner density structure due to a non-uniqueness of gravimetric inverse solutions, additional information is needed to constrain the gravimetric solutions. The methods applied in studies of the Earth's structure and processes thus should optimally combine various data and additional geophysical, geothermal or geochemical constraining information.

In recent years, global and regional gravity data have been used extensively to study the Moho density interface. However, classical isostatic models are typically not able to model realistically the actual Moho geometry, due to the fact that the actual isostatic balance depends on numerous factors, which could not accurately be described by isostatic theories. To overcome some theoretical deficiencies of classical isostatic models, the processing strategies based on combining gravity and seismic data (with additional constraining information) have been developed and applied. In this way, the gravitational data could improve the results over large parts of the world where seismic data are sparse or absent, while gravity also provide additional information over regions which are sufficiently covered by seismic surveys.

The gravimetric methods for studying the Earth's inner density structure comprise - in principle - two processing steps. The gravimetric forward modeling is first applied to model (and remove) the gravitational contribution of known density structures in order to uncover the gravitational signature of unknown (and sought) density structure or density interface. The gravimetric inverse methods are then used to interpret these unknown density structures based on analysis of refined gravity data (corrected for the gravitational contributions of known density structures). In both processing steps, seismic data can be used to constrain the gravimetric results. Such methods and their practical applications in context of modeling and interpreting the Earth's lithospheric structure and the Moho interface are presented and discussed here. Moreover, the examples of gravimetric methods for the interpretation of geodynamic processes related to the mantle convection are given, particularly studding the gravitational signature of the ocean-floor spreading and the sub-crustal stress field.

2. EARTH'S GRAVITY FIELD

The Earth's gravity field is commonly described by means of residual quantities of the gravity field, namely using the disturbing potential T, the gravity disturbance δg, and the gravity anomaly Δg. These residual quantities are obtained from the Earth's gravity field after subtracting the normal gravity field.

The disturbing potential T at an arbitrary point (r,Ω) is defined by (e.g., Heiskanen and Moritz 1967)

$$T(r,\Omega)=\frac{GM}{R}\sum_{n=0}^{\infty}\sum_{m=-n}^{n}\left(\frac{R}{r}\right)^{n+1}T_{n,m}\,Y_{n,m}(\Omega), \tag{2.1}$$

where GM is the geocentric gravitational constant, R is the Earth's mean radius, $Y_{n,m}$ are the (fully-normalized) surface spherical functions of degree *n* and order *m*, and $T_{n,m}$ are the (fully-normalized) numerical coefficients of the disturbing potential T. The coefficients $T_{n,m}$ are obtained from the GGM coefficients after subtracting the spherical harmonic coefficients of the GRS80 normal gravity field (Moritz 2000). The 3-D position is defined in the spherical coordinate system (r,Ω); where r is the spherical radius, and $\Omega=(\phi,\lambda)$ is the spherical direction with the spherical latitude ϕ and longitude λ.

By analogy with Eq. (2.1), the gravity disturbances δg and the gravity anomalies Δg are computed from the disturbing potential coefficients $T_{n,m}$ as follows (*ibid.*)

$$\delta g(r,\Omega)=\frac{GM}{R^2}\sum_{n=0}^{\infty}\sum_{m=-n}^{n}\left(\frac{R}{r}\right)^{n+2}(n+1)T_{n,m}\,Y_{n,m}(\Omega), \tag{2.2}$$

and

$$\Delta g(r,\Omega)=\frac{GM}{R^2}\sum_{n=0}^{\infty}\sum_{m=-n}^{n}\left(\frac{R}{r}\right)^{n+2}(n-1)T_{n,m}\,Y_{n,m}(\Omega). \tag{2.3}$$

3. EARTH'S DENSITY MODEL

To study the relation between the Earth's gravitational field and the Earth's inner density structure, the Earth's interior is divided into a finite number of volumetric mass density layers, which represent particular geological or

tectonic features. This description is then applied to compute and subsequently remove the gravitational contributions of known density structures from the Earth's gravitational field in order to reveal the gravitational signature of an unknown (and sought) density structure or density interface. Tenzer (2015) derived a generalized mathematical model of the Earth's density structure. This model is defined based on utilizing the spectral expressions for a 3-D density distribution within an arbitrary volumetric mass layer.

For this purpose, the actual density within an arbitrary volumetric mass layer is approximated by the laterally distributed radial density variation model using the following polynomial function (for each lateral column)

$$\rho_q(r,\Omega) \cong \rho_q\left(D_{U_q},\Omega\right) + {}_q\beta(\Omega)\sum_{i=1}^{I_q} {}_q\alpha_i(\Omega)\left(r-\mathrm{R}\right)^i$$
$$\mathrm{R}-D_{U_q}(\Omega) \geq r > \mathrm{R}-D_{L_q}(\Omega), \quad (q=1,2,\ldots Q), \tag{3.1}$$

where Q is a total number of volumetric mass layers used to describe the Earth's inner structure. Adopting the Earth's spherical approximation, the geometry of each volumetric layer is defined by depths D_U and D_L of the upper and lower bounds respectively. These depths are stipulated with respect to the Earth's mean radius R. For the upper and lower bounds located above the geoid surface (which is approximated by the sphere of radius R), the values D_U and D_L become negative. The 3-D density distribution in Eq. (3.1) is described by a (nominal) lateral density $\rho_q\left(D_{U_q},\Omega\right)$ at an upper bound D_{U_q} and a location Ω. A radial density change with respect to $\rho_q\left(D_{U_q},\Omega\right)$ is then described by the parameters ${}_q\beta$ and $\{{}_q\alpha_i : i=1,2,\ldots,I_q\}$, where I_q is a maximum order of the density function used to define a radial density change within a particular volumetric mass layer *q*.

For the 3-D density distribution model in Eq. (3.1), the spherical lower- and upper-bound density functions and their higher-order terms, i.e., $\{{}_q\mathrm{L}_\mathrm{n}^{(k+i)}, {}_q\mathrm{U}_\mathrm{n}^{(k+i)} : k=1,2,\ldots; i=0,1,\ldots,I_q;\ q=1,2,\ldots,Q\}$, are defined by (Tenzer et al. 2012b)

$$
{}_{q}\mathrm{L}_{\mathrm{n}}^{(k+i)}(\Omega)=\begin{cases}\dfrac{2n+1}{4\pi}\iint\limits_{\Phi}\rho_{q}\left(D_{U_q},\Omega'\right)D_{L_q}^{k}(\Omega')\mathrm{P}_{\mathrm{n}}(t)\,d\Omega' \\ =\displaystyle\sum_{\mathrm{m}=-\mathrm{n}}^{\mathrm{n}}{}_{q}\mathrm{L}_{\mathrm{n,m}}^{(k)}\mathrm{Y}_{\mathrm{n,m}}(\Omega) & i=0 \\ \dfrac{2n+1}{4\pi}\iint\limits_{\Phi}{}_{q}\beta(\Omega')\;{}_{q}\alpha_{i}(\Omega')D_{L_q}^{k+1}(\Omega')\mathrm{P}_{\mathrm{n}}(t)\,d\Omega' \\ =\displaystyle\sum_{\mathrm{m}=-\mathrm{n}}^{\mathrm{n}}{}_{q}\mathrm{L}_{\mathrm{n,m}}^{(k+i)}\,\mathrm{Y}_{\mathrm{n,m}}(\Omega) & i=1,2,\ldots,I_{q}\,,\end{cases}
\tag{3.2}
$$

and

$$
{}_{q}\mathrm{U}_{\mathrm{n}}^{(k+i)}(\Omega)=\begin{cases}\dfrac{2n+1}{4\pi}\iint\limits_{\Phi}{}_{q}\rho\left(D_{U_q},\Omega'\right)D_{U_q}^{k}(\Omega')\mathrm{P}_{\mathrm{n}}(t)\,d\Omega' \\ =\displaystyle\sum_{\mathrm{m}=-\mathrm{n}}^{\mathrm{n}}{}_{q}\mathrm{U}_{\mathrm{n,m}}^{(k)}\mathrm{Y}_{\mathrm{n,m}}(\Omega) & i=0 \\ \dfrac{2n+1}{4\pi}\iint\limits_{\Phi}{}_{q}\beta(\Omega')\;{}_{q}\alpha_{i}(\Omega')D_{U_q}^{k+i}(\Omega')\mathrm{P}_{\mathrm{n}}(t)\,d\Omega' \\ =\displaystyle\sum_{\mathrm{m}=-\mathrm{n}}^{\mathrm{n}}{}_{q}\mathrm{U}_{\mathrm{n,m}}^{(k+i)}\,\mathrm{Y}_{\mathrm{n,m}}(\Omega) & i=1,2,\ldots,I_{q}\,.\end{cases}
\tag{3.3}
$$

The methods for a spherical harmonic analysis of the Earth's density structure are applied to generate the coefficients ${}_{q}\mathrm{L}_{\mathrm{n,m}}^{(k+i)}$ and ${}_{q}\mathrm{U}_{\mathrm{n,m}}^{(k+i)}$ from discrete data of depth, thickness, and density distribution within a particular volumetric mass layer. These coefficients can then be used to compute the respective gravitational contributions (Chapter 6).

4. EXAMPLES OF DENSITY MODELS

To improve results of interpreting the marine gravity data, Gladkikh and Tenzer (2011) and Tenzer and Gladkikh (2014) developed density models of the seawater and marine sediments. Gu et al. (2014) applied these density models to predict density contrasts of the oceanic sedimentary basins with respect to the overlying seawater and the underlying bedrock. These density models were also utilized in marine gravity studies. Tenzer et al. (2011a)

compared the accuracy of the bathymetric-stripping gravity correction (i.e., the gravity correction due to the ocean density contrast) computed for the uniform and depth-dependent seawater density models. Tenzer et al. (2012a) and Tenzer and Novák (2012) applied the depth-dependent seawater density model in computing the bathymetric-stripping corrections to gravity and gravity gradient data. Chen et al. (2014) facilitated the density model of marine sediments in computing the sediment-stripping correction to marine gravity data. Tenzer et al. (2015b) applied these density models to compile the synthetic gravitational model of the oceanic lithosphere (Chapter 8). The density models of the seawater and marine sediments are presented in this chapter.

4.1 Seawater density model

The actual seawater density variations due to salinity, temperature, and pressure are typically at the interval from 1020 to 1050 kg m^{-3}, with most of this range being due to pressure. According to Garrison (2001), the surface seawater density varies between 1020 and 1029 kg m^{-3}. The largest vertical seawater density variations are within the pycnocline (i.e., the sub-surface layer with the largest seawater density gradient). These large density variations are mainly due to the decreasing seawater temperature with depth as well as a complex behavior of the seawater salinity at the upper oceanic layer. There are several other oceanographic phenomena, which contribute to the global seawater density variations such as the global oceanic circulation, the continental hydrology, and the ocean-floor relief.

When the actual seawater density distribution is approximated by a uniform density model, a relative inaccuracy up to 2% is expected in the gravimetric forward modeling of the bathymetric-stripping correction (cf. Tenzer et al. 2010a). It corresponds to errors in computed values of the gravitational potential and attraction (due to the ocean density contrast) to about 550 m^2s^{-2} and 17 mGal respectively. To reduce these errors, Gladkikh and Tenzer (2011) introduced a more accurate model of the seawater density. They used experimental data of the practical salinity, pressure, and temperature from the World Ocean Atlas 2009 (WOA09) and the World Ocean Circulation Experiment 2004 (WOCE04) to calculate the seawater density values according to TEOS-10 (Millero et al. 2008), and used these values to formulate

a theoretical model of the global seawater density distribution as a function of the oceanic depth (to account for density variations due to pressure) and the geographical latitude (to account for density variations due to salinity and temperature). They also incorporated the pycnocline density-gradient correction into the seawater density model. This correction approximates more closely density variations within the pycnocline caused by a combination of the decreasing temperature and the increasing salinity with depth.

As mentioned above, the seawater density variations are mainly due to pressure, while additional smaller density changes are caused by salinity and temperature changes. The global seawater temperature and salinity changes have a prevailing zonal (latitudinal) distribution (Stewart 2008). The seawater density variations ρ^{w} can then be described as a function of the oceanic depth d_w and the geographic latitude φ in the following form (Gladkikh and Tenzer 2011)

$$\rho^{w}(d_w,\varphi)=1000.0+\alpha(\varphi)+\beta(\varphi)d_w^{\vartheta(\varphi)}. \quad (4.1)$$

The parameters α, β, and ϑ in Eq. (4.1) were estimated by applying a least-squares analysis. These parameters are defined for the argument of latitude φ as follows

$$\alpha(\varphi)=27.91-2.06\exp\left[-\left(0.0161|\varphi|\right)^{5}\right], \quad (4.2)$$

$$\beta(\varphi)=0.00637+0.00828\exp\left[-\left(0.017|\varphi|\right)^{4.66}\right], \quad (4.3)$$

$$\vartheta(\varphi)=0.964-0.091\exp\left[-\left(0.016|\varphi|\right)^{5}\right]. \quad (4.4)$$

According to Eq. (4.1), a theoretical value of the surface seawater density at the equator equals 1027.91 kg m^{-3}. The parameter α describes a global latitudinal distribution of the surface seawater density, which increases towards higher latitudes. A change of the seawater density with depth is defined by the third term on the right-hand side of Eq. (4.1).

To improve the fit at shallow depths, the pycnocline-corrected seawater density model was proposed in the following form (Gladkikh and Tenzer 2011)

$$\rho^{w}(d_w,\varphi)=1000+\beta(\varphi)d_w^{\vartheta(\varphi)}+\alpha(\varphi)\left\{\mu(\varphi)+\frac{1-\mu(\varphi)}{2}\left[1+\tanh\left(0.00988\,d_w-1.01613\right)\right]\right\}, \quad (4.5)$$

where the latitude-dependent parameter μ reads

$$\mu(\varphi) = 0.928 - 0.079\cos 0.053\varphi\,. \tag{4.6}$$

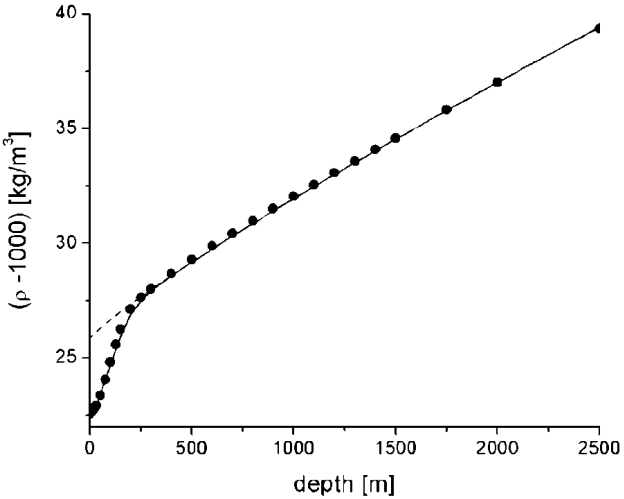

Fig. 4.1 *Fit of the latitude-averaged seawater density data by the seawater density model (dashed line) in Eq. (4.1) and the pycnocline-corrected seawater density model (solid line) in Eq. (4.5).*

The approximation of the actual seawater density distribution by a mean value yields relative errors up to 2%. A theoretical model defined in terms of the depth and latitudinal seawater density variations (Eq. 4.1) approximates experimental data with a relative accuracy better than 0.45%. When incorporating the pycnocline density-gradient correction to the seawater density model (Eq. 4.5), a relative accuracy further improved to about 0.25%, especially within the pycnocline (see Fig. 4.1).

The analysis revealed that the seawater densities of experimental data vary between 1020 and 1055 kg m^{-3} within the depth range 6 km. The corresponding mean seawater density is 1038.5±2.4 kg m^{-3}. The surface seawater densities of experimental data vary from 1022 to 1027.3 kg m^{-3}, with a mean 1024.8±3.0 kg m^{-3}. This mean value closely agrees with the mean surface seawater density 1025.3 kg m^{-3} computed according to Eq. (4.5).

4.2 Marine sediment density model

The density heterogeneities of marine sediments depend on their physical properties and mineral composition, which are the result of a complex interaction among geological, oceanographic, and biological processes (e.g., Hüneke and Mulder 2011). Several authors developed and applied more complex density models taking into consideration a particular sediment type and its specific physical properties such as porosity and compaction (e.g., Hamilton and Menard 1956, Hamilton 1976, Cowie and Karner 1990, and Sykes 1996). Analyzing the density samples from the Deep Sea Drilling Project (DSDP), Tenzer and Gladkikh (2014) developed a density model of marine sediments ρ^s as a function of the ocean-floor depth D_w and the sediment thickness d_s in the following form

$$\rho^s(d_s, D_w) = [1.66 \pm 0.02] - D_w \left[(5.1 \pm 0.5) \times 10^{-5}\right] + [0.0037 \pm 0.0002]\, d_s^{[0.766 \pm 0.007]}. \quad (4.7)$$

The transportation distance, depositional environment conditions (depth, temperature, concentrations of dissolved gas, calcium carbonate, and silica), and ocean fertility control both, the sediment structure and sedimentation process. Among these factors, the lateral density distribution depends primarily on a mineral composition and transportation distance. Light and fine particles are transported at longer distances. Consequently, there is a clear pattern in the size distribution, for instance, of lithogenous sediments in the oceans (forming about 70% of total volume of marine sediments). Coarse particles (gravels, sands) form mostly near-shore deposits, while the grain-size typically decreases offshore with clays occupying the deep-ocean basins. This might explain a prevailing trend of the decreasing upper-sediment density with the increasing ocean-floor depth (see Fig. 4.2). The increasing sediment density with sediment depth (see Fig. 4.3) is explained by the compaction and further lithification.

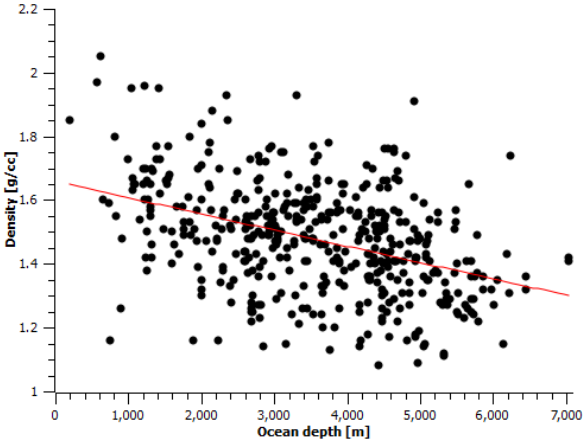

Fig. 4.2 *Relation between the upper-sediment density (for d_s<50 m) and the ocean-floor depth. Theoretical density values (red line) were calculated according to Eq. (4.7).*

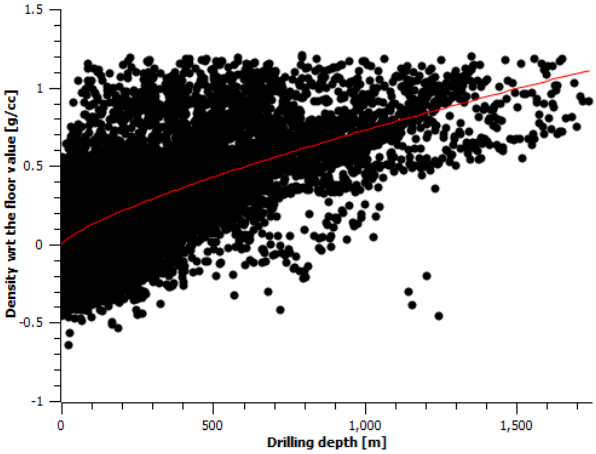

Fig. 4.3 *Relation between the marine sediment density and the sediment depth. Theoretical density values (red line) were calculated according to Eq. (4.7).*

5. EARTH'S CRUSTAL DENSITY MODEL

Chen and Tenzer (2015) utilized the expressions for a spherical harmonic analysis of crustal density structures (Chapter 3) to generate the Earth's Spectral Crustal Model 180 (ESCM180) with a spectral resolution complete to a spherical harmonic degree 180 (which corresponds to a half-wavelength of 1

arc-deg, or about 100 km at the equator). They used the ETOPO1 topographic and bathymetric data (Amante and Eakins 2009), the GOCO-03S geoid model (Mayer-Guerr et al. 2012), the Kort and Matrikelstyrelsen (KMS) ice-thickness data for Greenland (Ekholm 1996), the updated ice-thickness data for Antarctica assembled by the BEDMAP project (Lythe et al. 2001), and the CRUST1.0 sediment and consolidated crustal data (Laske and Masters 1997, and Laske et al. 2012). Moreover, the density models of seawater and marine sediments (Chapter 4) were adopted to represent the density distribution within the ocean and marine sediment layers.

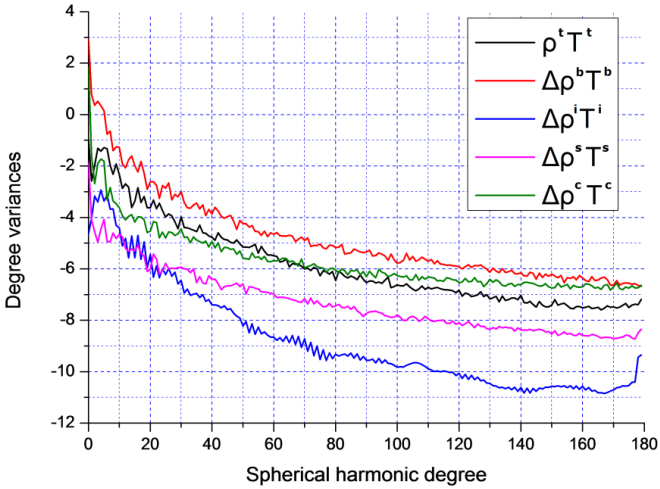

Fig. 5.1 *Power spectrum of the ESCM180 crustal density components. The crustal density components were evaluated from the ESCM180 coefficients as a product ρT or $\Delta\rho T$; where ρ and $\Delta\rho$ is the density or density contrast respectively, and T is the thickness of crustal layers (t - topography, b - bathymetry, i - ice, s - sediment, c - consolidated crust). Log scale is used for vertical axis.*

The spectrum of the ESCM180 components is plotted in Fig. 5.1. The ocean density contrast has the largest signal among the ESCM180 components at the whole investigated spectrum (up to degree 180). The topographic and sediment layers have a similar energy at the medium wavelengths (at degrees 60 to 85). The signal of the ice density contrast prevails over the signal of the sediment density contrast at the long wavelengths up to degree 10, while both these signals are very similar at degrees from 10 to 25. Above this

interval, the signal of the ice density contrast becomes the smallest (among all components). This behavior is explained by a more concentrated spatial distribution of the glacial ice in Greenland and Antarctica. The global sediment distribution is, on the other hand, much more irregular and characterized by large variations in its thickness and density. Therefore, the signal of the sediment density contrast prevails at the medium-to-higher frequencies, while the ice density contrast has a stronger signal at the longer wavelengths.

The ESCM180 parameters were further used to estimate average densities of the Earth's crustal structures. The analysis revealed that the average crustal density including the seawater is 2490 kg m^{-3}, while the solid crust density (i.e., excluding the seawater) is 2830 kg m^{-3}. These estimates were obtained by applying a spatial average operator over crustal layers (while taking into consideration the convergence of meridians). The average continental crustal density including continental margins (which comprise igneous, sedimentary, and metamorphic rocks) is 2790 kg m^{-3}. This value differs about 1.6% from the value 2835 kg m^{-3} reported by Christensen and Mooney (1995). These two density estimates of the whole continental crust are obviously larger than the average density of the upper continental crust 2670 kg m^{-3} (mentioned by Hinze 2003) due to the increasing density within deeper crustal structures.

The oceanic crust (composed primarily of mafic rocks) is typically heavier than the continental crust (e.g., Rogers et al. 2008). The analysis revealed that the average density of the ESCM180 oceanic crust (without the seawater, but including marine sediments) is 2860 kg m^{-3}. This value is obviously smaller than the average density of the oceanic crust (without marine sediments) 2890 kg m^{-3} estimated by Carlson and Raskin (1984). Tenzer and Gladkikh (2014) confirmed a similar value of the average density of the oceanic crust (without marine sediments) 2900 kg m^{-3}, based on analysis of the DSDP marine bedrock density samples. They also found that the average density of the DSDP marine sediments data is 1700 kg m^{-3}. Sykes (1996) reported the average density of marine sediments between 1700 and 1950 kg m^{-3}.

6. GRAVIMETRIC FORWARD MODELING

Tenzer et al. (2012b, 2012d) derived generic expressions for computing the gravitational field quantities generated by an arbitrary volumetric mass layer with a variable depth and thickness having a 3-D density (or density contrast)

distribution (Chapter 3). The gravitational attraction g (defined approximately as a negative radial derivative of the gravitational potential V) reads

$$g(r,\Omega) \cong -\frac{\partial V(r,\Omega)}{\partial r} = \frac{\mathrm{GM}}{\mathrm{R}^2} \sum_{n=0}^{\bar{n}} \sum_{m=-n}^{n} \left(\frac{\mathrm{R}}{r}\right)^{n+2} (n+1)\mathrm{V}_{\mathrm{n,m}}\ \mathrm{Y}_{\mathrm{n,m}}(\Omega), \qquad (6.1)$$

where $\bar{n}$ is the upper summation index of spherical harmonics. The potential coefficients $\mathrm{V}_{\mathrm{n,m}}$ are given by

$$\mathrm{V}_{\mathrm{n,m}} = \frac{3}{2n+1} \frac{1}{\bar{\rho}^{\mathrm{Earth}}} \sum_{i=0}^{I} \left(\mathrm{Fl}_{\mathrm{n,m}}^{(\mathrm{i})} - \mathrm{Fu}_{\mathrm{n,m}}^{(\mathrm{i})}\right), \qquad (6.2)$$

where $\bar{\rho}^{\mathrm{Earth}}$ is the Earth's mean density. The numerical coefficients $\{\mathrm{Fl}_{\mathrm{n,m}}^{(\mathrm{i})}, \mathrm{Fu}_{\mathrm{n,m}}^{(\mathrm{i})} : i = 0,1, ..., I\}$ are defined as follows

$$\mathrm{Fl}_{\mathrm{n,m}}^{(\mathrm{i})} = \sum_{k=0}^{n+2} \binom{n+2}{k} \frac{(-1)^k}{k+1+i} \frac{\mathrm{L}_{\mathrm{n,m}}^{(k+1+i)}}{\mathrm{R}^{\mathrm{k+1}}}, \quad \mathrm{Fu}_{\mathrm{n,m}}^{(\mathrm{i})} = \sum_{k=0}^{n+2} \binom{n+2}{k} \frac{(-1)^k}{k+1+i} \frac{\mathrm{U}_{\mathrm{n,m}}^{(k+1+i)}}{\mathrm{R}^{\mathrm{k+1}}}. \quad (6.3)$$

The terms $\sum_{\mathrm{m=-n}}^{\mathrm{n}} \mathrm{L}_{\mathrm{n,m}}\, \mathrm{Y}_{\mathrm{n,m}}$ and $\sum_{\mathrm{m=-n}}^{\mathrm{n}} \mathrm{U}_{\mathrm{n,m}}\, \mathrm{Y}_{\mathrm{n,m}}$ define the spherical lower-bound and upper-bound density functions L_{n} and U_{n} of degree n. From Eqs. (3.2) and (3.3), these spherical functions and their higher-order terms, i.e., $\{\mathrm{L}_{\mathrm{n}}^{(k+1+i)}, \mathrm{U}_{\mathrm{n}}^{(k+1+i)} : k = 0,1,\ldots; i = 1,2, ..., I\}$, are obtained in the following form

$$\mathrm{L}_{\mathrm{n}}^{(k+1+i)}(\Omega) = \begin{cases} \dfrac{2n+1}{4\pi} \iint_{\Phi} \rho(D_U, \Omega') D_L^{k+1}(\Omega') \mathrm{P}_{\mathrm{n}}(t)\, d\Omega' \\ = \sum_{\mathrm{m=-n}}^{\mathrm{n}} \mathrm{L}_{\mathrm{n,m}}^{(k+1)}\, \mathrm{Y}_{\mathrm{n,m}}(\Omega) \qquad\qquad i = 0 \\ \\ \dfrac{2n+1}{4\pi} \iint_{\Phi} \beta(\Omega') \alpha_i(\Omega') D_L^{k+1+i}(\Omega') \mathrm{P}_{\mathrm{n}}(t)\, d\Omega' \\ = \sum_{\mathrm{m=-n}}^{\mathrm{n}} \mathrm{L}_{\mathrm{n,m}}^{(k+1+i)}\, \mathrm{Y}_{\mathrm{n,m}}(\Omega) \qquad\qquad i = 1,2,..., I, \end{cases} \qquad (6.4)$$

and

$$
\mathrm{U}_{\mathrm{n}}^{(k+1+i)}(\Omega)=\begin{cases}
\dfrac{2n+1}{4\pi}\iint_{\Phi}\rho(D_U,\Omega')D_U^{k+1}(\Omega')\mathrm{P}_{\mathrm{n}}(t)\,d\Omega' \\
=\sum_{\mathrm{m}=-\mathrm{n}}^{\mathrm{n}}\mathrm{U}_{\mathrm{n,m}}^{(k+1)}\,\mathrm{Y}_{\mathrm{n,m}}(\Omega) & i=0 \\
 & \\
\dfrac{2n+1}{4\pi}\iint_{\Phi}\beta(\Omega')\,\alpha_i(\Omega')D_U^{k+1+i}(\Omega')\mathrm{P}_{\mathrm{n}}(t)\,d\Omega' \\
=\sum_{\mathrm{m}=-\mathrm{n}}^{\mathrm{n}}\mathrm{U}_{\mathrm{n,m}}^{(k+1+i)}\,\mathrm{Y}_{\mathrm{n,m}}(\Omega) & i=1,2,\ldots,I.
\end{cases}
\tag{6.5}
$$

The generic expressions for computing the gravitational field quantities presented in this chapter can readily be simplified for the radial, lateral or uniform density models.

7. GRAVITATIONAL FIELD OF CRUSTAL STRUCTURES

Tenzer et al. (2012b, 2012e) and Novák et al. (2013) applied the expressions presented in Chapter 6 in the gravimetric forward modeling of crustal density structures. Tenzer et al. (2015e) used the ESCM180 coefficients to compute the gravitational contributions of major crustal density structures. They also investigated the spatial and spectral characteristics of the consolidated crust-stripped gravity disturbances δg^{cs} (Tenzer et al. 2009a) computed from the gravity disturbances δg according to the following scheme

$$
\delta g^{cs}=\delta g-g^{\mathrm{T}}-g^{\mathrm{B}}-g^{\mathrm{I}}-g^{\mathrm{S}}-g^{\mathrm{C}}, \tag{7.1}
$$

where g^{T} is the topographic gravity correction, and g^{B}, g^{I}, g^{S} and g^{C} are, respectively, the stripping gravity corrections due to density contrasts of the ocean (bathymetry), ice, sediments and consolidated crust. Global maps of the gravity corrections and the (step-wise) corrected gravity disturbances are presented in Figs. 7.1 and 7.2. The statistical summaries of these results are given in Tables 7.1 and 7.2.

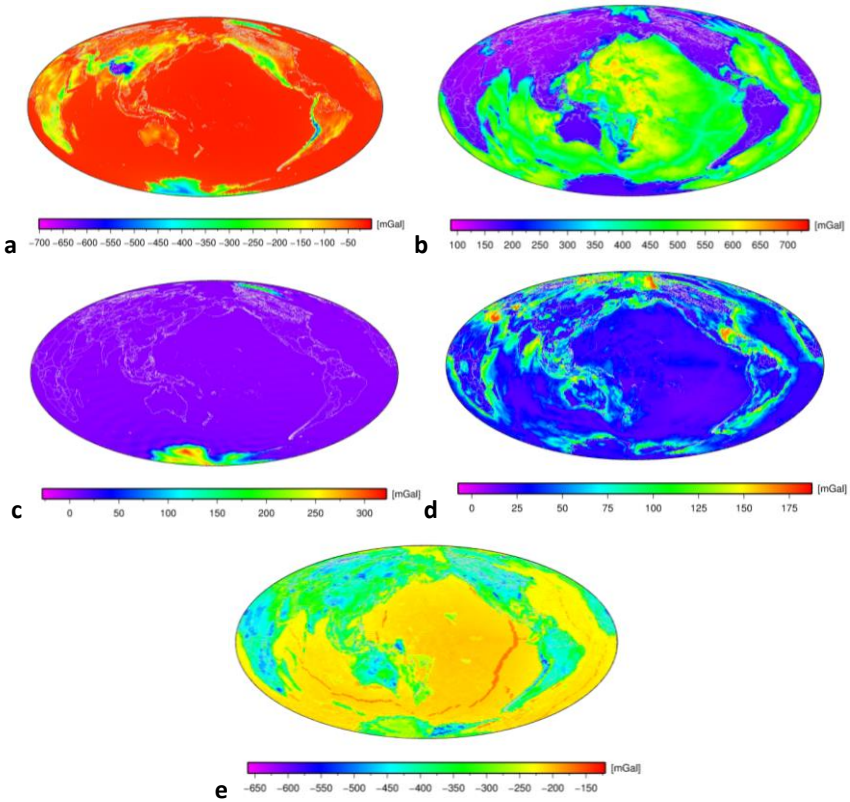

Fig. 7.1 *Global maps of the gravity corrections (mGal): (**a**) the topographic correction g^T, (**b**) the bathymetric-stripping correction g^B, (**c**) the ice-striping correction g^I, (**d**) the (complete) sediment-stripping correction g^S, and (**e**) the (complete) consolidated crust-stripping correction g^C.*

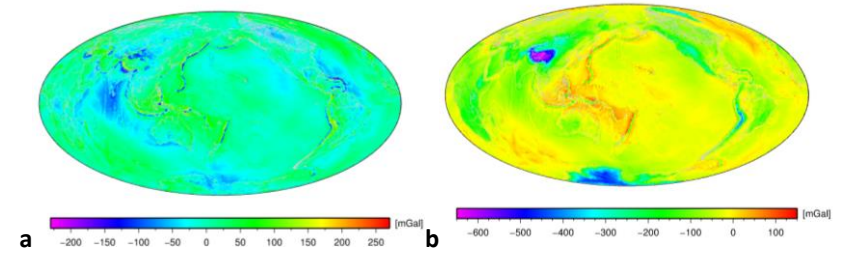

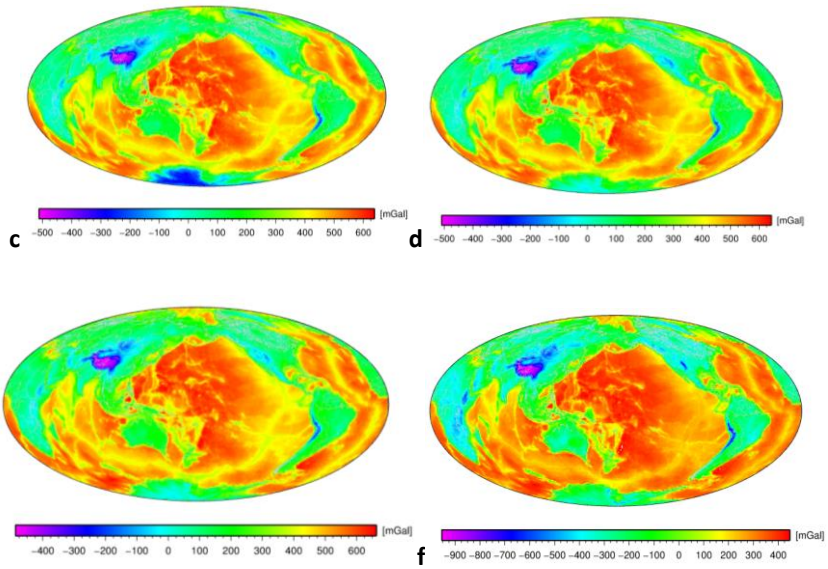

Fig. 7.2 *Global maps of the (step-wise) corrected gravity disturbances (mGal): (**a**) the GOCE-03S gravity disturbances δg, (**b**) the topography-corrected gravity disturbances δg^{T}, (**c**) the topography-corrected and bathymetry-stripped gravity disturbances δg^{TB}, (**d**) the topography-corrected and bathymetry- and ice-stripped gravity disturbances δg^{TBI}, (**e**) the topography-corrected and bathymetry- and ice- and sediments-stripped gravity disturbances δg^{TBIS}, and (**f**) the consolidated crust-stripped gravity disturbances δg^{cs}.*

Table 7.1 *Statistics of the gravity corrections (mGal): the topographic g^{T}; the bathymetric-stripping g^{B}; the ice-striping g^{I}; the upper, middle, and lower sediment-stripping g^{uS}, g^{mS}, and g^{lS}; and the upper, middle, and lower consolidated crust-stripping g^{uC}, g^{mC}, and g^{lC}.*

Gravity corrections	**Min** [mGal]	**Max** [mGal]	**Mean** [mGal]	**STD** [mGal]
g^{T}	-701	5	-71	104
g^{B}	89	725	332	165
g^{I}	-27	311	25	61
g^{uS}	-3	105	34	21
g^{mS}	-17	87	11	14
g^{lS}	-5	29	1	2
g^{uC}	-141	52	-20	24
g^{mC}	-199	-22	-71	35
g^{lC}	-526	-106	-202	40

Table 7.2 *Statistics of the (step-wise) corrected gravity disturbances (mGal): the GOCE-03S gravity disturbances δg, the topography-corrected gravity disturbances δg^{T}; the topography-corrected and bathymetry-stripped gravity disturbances δg^{TB}; the topography-corrected and bathymetry- and ice-stripped gravity disturbances δg^{TBI}; the topography-corrected and bathymetry- and ice- and sediment-stripped gravity disturbances δg^{TBIS} (including intermediate results: δg^{TBIuS} - after applying the upper-sediment-stripping correction to δg^{TBI}, and $\delta g^{TBIuSmS}$ - after applying the upper- and middle-sediment stripping corrections to δg^{TBI}); and the consolidated crust-stripped gravity disturbances δg^{cs} (including the intermediate results: δg^{TBISuC} - after applying the upper-crust-stripping correction to δg^{TBIS}, and $\delta g^{TBISuCmC}$ - after applying the upper- and middle-crust-stripping corrections to δg^{TBIS}).*

Gravity disturbance	**Min** [mGal]	**Max** [mGal]	**Mean** [mGal]	**STD** [mGal]
δg	-229	257	-1	30
δg^{T}	-648	167	-72	107
δg^{TB}	-511	634	260	233
δg^{TBI}	-508	638	285	202
δg^{TBIuS}	-494	664	319	203
$\delta g^{TBIuSmS}$	-487	669	330	200
δg^{TBIS}	-486	669	331	200
δg^{TBISuC}	-579	667	311	219
$\delta g^{TBISuCmC}$	-709	625	240	249
δg^{cs}	-954	460	38	275

As seen in Fig. 7.2a, the GOCO-03S gravity disturbances globally vary mostly within ±250 mGal. This small range of gravity disturbances indicates that the Earth's lithosphere is in a relatively good isostatic balance at the long-to-medium wavelengths. The application of the topographic gravity correction (Fig. 7.1a) exhibited the isostatic signature in the gravity data over major orogens, marked there by large negative values of the gravity disturbances (see Fig. 7.2b). The application of the bathymetric-stripping gravity correction (Fig. 7.1b) significantly changed a spatial pattern of the marine gravity disturbances, revealing the gravitational signature of the ocean-floor relief (see Fig. 7.2c). The application of the ice-stripping gravity correction (Fig. 7.1c) modified the gravity disturbances in Greenland and Antarctica (Tenzer et al. 2010b), particularly over areas with the largest glacial ice cover (see Fig. 7.2d). The application of the sediment-stripping gravity correction (Fig. 7.1d) slightly changed a spatial pattern of the gravity disturbances over large continental

sedimentary basins and to some extent also enhanced the contrast between the continental and oceanic crustal structures along the continental margins, especially over the largest sedimentary accumulations of deep-sea fans (i.e., large marine sediment accumulations deposited on the slope and adjacent sea-floor, originated during the ice-age climatic episodes) and the sediment discharge of large rivers (see Fig. 7.2e). The consolidated crust-stripped gravity disturbances, obtained after applying the stripping gravity correction due to remaining crustal density heterogeneities (Fig. 7.1e), are mostly positive over oceans and negative over continents (see Fig. 7.2f). Their gravity maxima correspond with locations of the old oceanic lithosphere, while the corresponding gravity maxima are seen over large orogens. It is worth mentioning that the atmospheric gravity correction was not applied here, because is completely negligible in context of this study. Tenzer et al. (2009c) demonstrated that this gravity correction globally varies only between -0.18 and 0.03 mGal.

As seen in the global gravity maps (Fig. 7.2), the successive application of the gravity corrections revealed a gravitational signature, which spatially closely resembles major features of the solid topography and the Moho geometry. The spatial correlation between the (step-wise) corrected gravity disturbances and the crustal geometry (i.e., the solid topography and the Moho geometry) is summarized in Table 7.3.

Table 7.3 *Correlations of the step-wise corrected gravity disturbances with the ESCM180 solid topography and the CRUST1.0 Moho geometry.*

Gravity disturbances	Correlation	
	Solid topography	Moho geometry
δg	-0.01	-0.09
δg^{T}	-0.55	-0.68
δg^{TB}	-0.89	-0.95
δg^{TBI}	-0.92	-0.97
δg^{TBIS}	-0.94	-0.97
δg^{cs}	-0.95	-0.98

The degree-correlation coefficients were further calculated to assess the spectral correlation pattern between the (step-wise) corrected gravity disturbances and the crustal geometry. The spectral correlations of the (step-wise) corrected gravity disturbances with the crustal geometry (up to degree 180) are shown in Fig. 7.3.

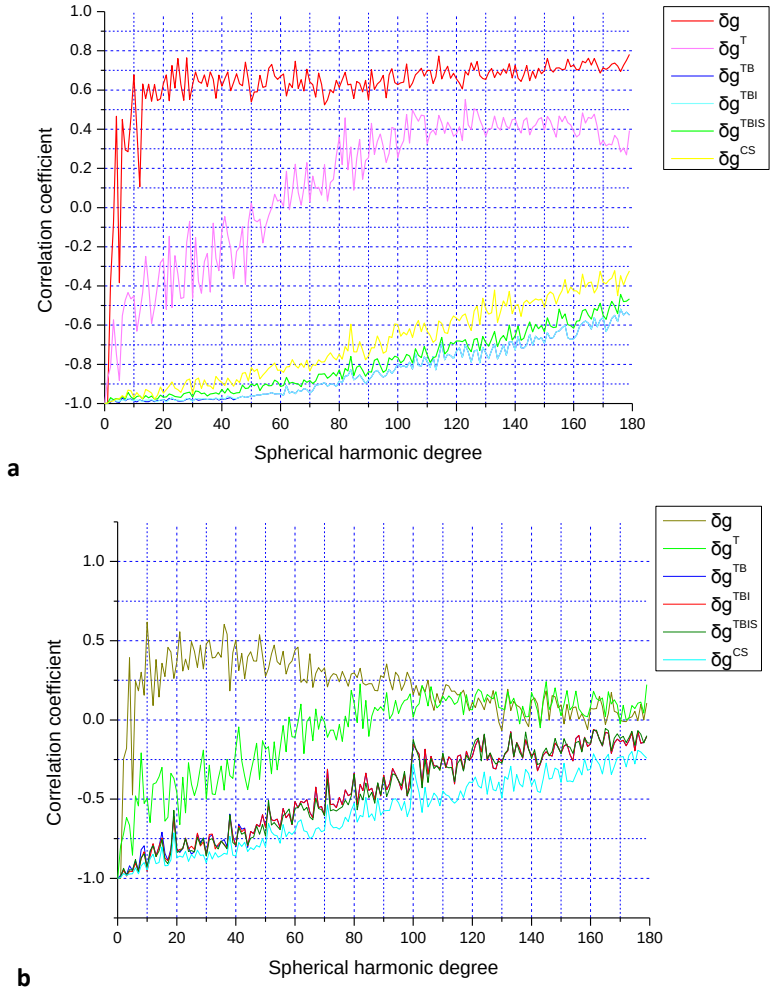

Fig. 7.3 *Degree-correlation spectrum of the step-wise corrected gravity disturbances with: (**a**) the ESCM180 solid topography, and (**b**) the CRUST1.0 Moho geometry.*

Despite the consolidated crust-stripped gravity disturbances are highly spatially correlated with the Moho geometry (cf. Table 7.3), this correlation prevails at the long wavelengths, while attenuates significantly at higher degrees of the gravitational spectrum (Tenzer et al. 2009b). The signature of the Moho geometry is thus prominent mainly at the long-to-medium wavelengths of the gravitational spectrum (cf. Fig. 7.3b), while the higher-degree spectrum is dominated mainly by the signature of the solid topography (cf. Fig. 7.3.a). This finding agrees with the fact that more detailed topographic features and anomalous crustal density structures are not fully isostatically compensated.

8. GRAVITATIONAL MODEL OF OCEANIC LITHOSPHERE

Tenzer et al. (2015d) compiled the synthetic gravitational model of the oceanic lithosphere over the world's oceans. This synthetic model describes the gravitational signature of the oceanic lithosphere attributed to the conductive cooling and thermal contraction of the oceanic lithosphere, which is isostatically compensated by the oceanic deepening (e.g., Williams 1975, and Parsons and Sclater 1977). This model was established based on finding that a spatial pattern of the mantle gravity disturbances (corrected for the long-wavelength gravitational contribution of deep mantle heterogeneities) over the world's oceans reflects mainly the compositional and thermal structure of the oceanic lithosphere (cf. Tenzer et al. 2012e, 2012f, 2013), except for some systematic discrepancies which could not accurately be described by a simple analytical function.

To unmask the gravitational signature of the oceanic lithosphere in marine gravity data, the gravitational contributions of anomalous crustal density structures were first subtracted from the gravity disturbances. This numerical procedure yields the consolidated crust-stripped gravity disturbances (Tenzer at al. 2009a, 2015e; see also Eq. 7.1). As demonstrated in Chapter 7, these gravity data comprise mainly the gravitational signatures of the Moho geometry and the mantle density heterogeneities. The gravitational contribution of the Moho geometry was further removed from the consolidated crust-stripped gravity disturbances in order to enhance the gravitational signature of the mantle. The resulting mantle gravity disturbances comprise the gravitational signal of the lithospheric mantle,

which is superposed over the (long-wavelength) gravitational signal of the sub-lithospheric mantle. To enhance the gravitational signature of the lithospheric mantle, the gravitational contribution of the sub-lithospheric mantle was finally subtracted from the mantle gravity disturbances. The computation of the long-wavelength contribution of the sub-lithospheric mantle was realized according to Bagherbandi and Sjöberg (2012b). They proposed a procedure of treating the gravitational signal of the whole mantle in solving the Vening Meinesz-Moritz inverse problem of isostasy by applying the method of Eckhardt (1983) and Bowin et al. (1986). The resulting gravity data were described analytically.

Tenzer et al. (2015d) demonstrated that the gravitational changes due to the lithospheric conductive cooling can be described as a function of the ocean-floor age in the following form

$$g'^{ol}(a) = 827 + 52.6\ln(1+a), \tag{8.1}$$

where g'^{ol} is the predicted value of the gravitational contribution of the oceanic lithosphere g^{ol} (mGal), and a is the ocean-floor age (Myr). This relation is illustrated in Fig. 8.1. The differences between the actual and theoretical values $g^{ol} - g'^{ol}(a)$ were then used to find an additional systematic trend with respect to the oceanic deepening caused by the lithospheric thermal contraction. A following linear trend was found (*ibid.*)

$$g^{ol} - g'^{ol} = -183 + 0.044\, D_w, \tag{8.2}$$

where D_w denotes the bathymetric depth (in m). This relation is shown in Fig. 8.2.

Combining Eqs. (8.1) and (8.2), the gravitational model of the oceanic lithosphere was obtained in the following form

$$\bar{g}^{ol}(a, D_w) = 644 + 52.6\ln(1+a) + 0.044\, D_w. \tag{8.3}$$

The gravitational field of the oceanic lithosphere reflects its thermal state. The gravitational signature of the ocean-floor spreading was explained by an increasing density with age due to the lithospheric conductive cooling (Fig. 8.1). This increasing density translates into the increasing gravitational signal with the gravitational minima over the mid-oceanic ridges and the gravitational maxima over the oceanic subduction zones. The gravitational signature of the lithospheric thermal contraction, which is isostatically

compensated by the oceanic deepening, was confirmed by a spatial correlation between the gravitational field and the ocean-floor depth (Fig. 8.2).

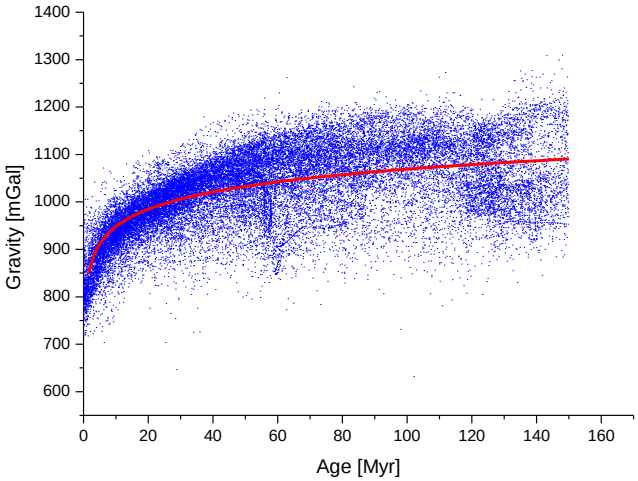

Fig. 8.1 *Scatter plot between the gravitational contribution of the oceanic lithosphere and the ocean-floor age. Approximation function is defined in Eq. (8.1).*

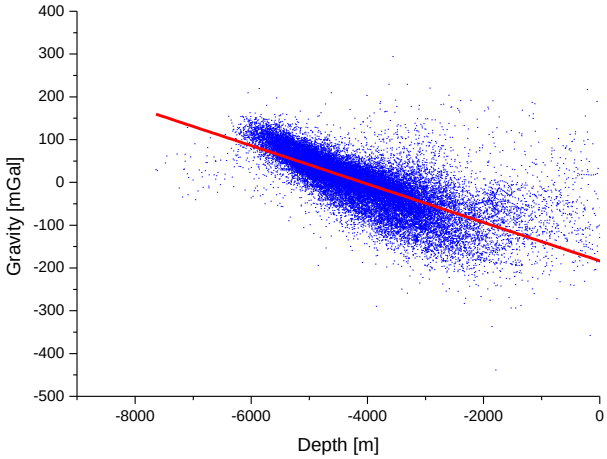

Fig. 8.2 *Scatter plot between the (age-adjusted) gravitational contribution of the oceanic lithosphere and the ocean-floor depth. Approximation function is defined in Eq. (8.2).*

9. GRAVIMETRIC MOHO RECOVERY

Seismic data are primarily used in geophysical studies investigating the Moho geometry. In the absence or a low coverage of seismic data, the gravimetric or combined gravimetric-seismic methods can be applied. Several different gravimetric methods for finding the Moho depth have been developed and applied in global and regional studies. Examples of gravimetric methods include, but are not limited to, studies by Čadek and Martinec (1991), Braitenberg and Zadro (1999), Arabelos et al. (2007), Sjöberg (2009), Braitenberg et al. (2010), Sampietro (2011), Eshagh et al. (2011), Bagherbandi and Eshagh (2011, 2012), Sampietro et al. (2013), Bagherbandi et al. (2013, 2015), Bagherbandi and Tenzer (2013), and Tenzer et al. (2015f). These gravimetric methods are typically formulated for a chosen isostatic scheme. The Pratt's isostatic model is based on the assumption of a variable compensation density (Pratt 1855), while a variable compensation depth is considered in the Airy's isostatic model (Airy 1855). Vening Meinesz (1931) modified the Airy-Heiskanen's theory by introducing a regional isostatic compensation based on a thin plate lithospheric flexure model. The regional compensation model was later adopted in the Parker-Oldenburg's isostatic method (Oldenburg 1974). Moritz (1990) utilized the Vening Meinesz's isostatic problem for the Moho depth determination. Sjöberg (2009, 2013) reformulated the Moritz's problem, called the Vening Meinesz-Moritz's (VMM) inverse problem of isostasy, by means of solving a non-linear Fredholm integral equation of the first kind.

The isostatic balance depends on the loading and effective elastic thickness, rigidity, rheology of the lithosphere, and viscosity of the asthenosphere. Moreover, the glacial isostatic adjustment, the present-day glacial melting, plate tectonics, the mantle convection, and other factors contribute to the overall isostatic balance. Kaban et al. (1999), for instance, demonstrated that the isostatic mass balance takes place not only within the crust, but essentially within the whole lithosphere (see also Kaban et al. 2004, and Tenzer et al. 2009a, 2012e). Isostatic gravity data also contain the long-wavelength signature of thermal and compositional structure of the mantle, which are typically not taken into consideration in classical isostatic models. Furthermore, these isostatic models often assume only a constant

compensation depth or density. However, the results of seismic studies revealed that both, the Moho depth and density contrast vary significantly (e.g., Geiss 1987, Martinec 1994, Kaban et al. 2003, and Sjöberg and Bagherbandi 2011). To overcome some theoretical deficiencies of classical isostatic models, the gravimetric methods for a Moho recovery should optimally combine the gravity and seismic data with additional constraining information. A combined data-processing strategy for the Moho recovery was applied, for instance, by Braitenberg and Zadro (1999). They proposed a method based on the iterative 3-D gravity inversion with integrated seismic data. Sjöberg and Bagherbandi (2011) developed and applied a least-squares approach, which combined seismic and gravity data in the VMM isostatic inverse scheme for a simultaneous estimation of the Moho depth and density contrast. They also presented and applied the non-isostatic correction term to account for discrepancies between the isostatic and seismic models (cf. Bagherbandi and Sjöberg 2012b, and Bagherbandi et al. 2013, 2015).

The isostatic problems are commonly formulated in terms of the isostatic gravity anomalies. Vajda et al. (2007) argued that these definitions in terms of the gravity disturbances are theoretically more appropriate. Following this concept, Tenzer and Bagherbandi (2012) reformulated the VMM isostatic model by means of the isostatic gravity disturbances (see also Bagherbandi et al. 2013). They also demonstrated that the Moho depths determined using the isostatic gravity disturbances better agree with a global seismic model than those obtained from the isostatic gravity anomalies. Sjöberg (2013) summarized definitions of the isostatic gravity field quantities for the potential and gravity data types. He also gave a theoretical explanation to the numerical results of Tenzer and Bagherbandi (2012).

Tenzer (2013a) and Tenzer and Chen (2014a, 2014b) developed a novel approach to determine the Moho depths using the global and regional gravitational and crustal structure models, and Tenzer (2013b) modified this approach for a determination of the Moho density contrast. This approach utilizes a relation between the consolidated crust-stripped gravity disturbances and the Moho depths (by means of a non-linear Fredholm's integral equation of the first kind). As it was demonstrated in Chapter 8, the consolidated crust-stripped gravity disturbances have a maximum spatial correlation with the Moho geometry. These gravity data are thus the most

suitable for the gravimetric Moho recovery. Since the relation between the consolidated crust-stripped gravity disturbances and the Moho depth is non-linear, a linearization is applied in order to establish a system of linearized observation equations for solving the gravimetric Moho inversion problem. The applied linearization procedure involves a compensation scheme, which minimizes a spatial correlation between the mantle gravity disturbances and the Moho geometry in order to obtain the initial solution that closely approximates the *a priori* Moho model. The mantle gravity disturbances are then used as input gravity data in an iterative process of solving the inverse problem for finding the Moho-depth corrections. Tenzer and Chen (2014a) defined this functional model in the spectral domain for global applications. Tenzer and Chen (2014b) derived the respective expressions in the spatial domain for a regional Moho inversion. Despite the consolidated crust-stripped gravity disturbances have a maximum correlation with the Moho geometry these gravity data still contain the gravitational signature of the (unmodelled) mantle density heterogeneities. To account for the density variations within the upper mantle, Tenzer et al. (2015f) reformulated the gravimetric inverse problem for a Moho recovery by assuming a variable Moho density contrast $\Delta\rho^{c/m}(\Omega)=\rho^{m}(\Omega)-\rho^{c}$, which is defined as the difference between the (laterally varying) upper mantle density ρ^{m} and the (constant) crustal density ρ^{c}. According to their definition, the linearized relation between the (known) mantle gravity disturbances $\delta g^{m,\Delta\rho}$ and the (unknown) Moho depths reads

$$\delta g^{m,\Delta\rho}(r,\Omega)=\frac{GM}{R^{2}}\sum_{n=0}^{\bar{n}}\left(\frac{R}{r}\right)^{n+2}\sum_{m=-n}^{n}F_{n,m}^{\Delta\rho\delta M}\,Y_{n,m}(\Omega). \tag{9.1}$$

The Moho-depth correction coefficients $F_{n,m}^{\Delta\rho\delta M}$ is given by

$$F_{n,m}^{\Delta\rho\delta M}=\frac{3}{\bar{\rho}^{\,Earth}}\frac{n+1}{2n+1}\sum_{k=0}^{n+2}\binom{n+2}{k}\frac{(-1)^{k}}{R^{k+1}}\left(\Delta\rho^{c/m}\delta M\right)_{n,m}^{(k)}, \tag{9.2}$$

where the coefficients $\{(\Delta\rho\delta M)_{n,m}^{(k)}:k=1,2,\ldots\}$ are defined by

$$\begin{aligned}(\Delta\rho\delta M)_{n}^{(k)}&=\frac{2n+1}{4\pi}\iint_{\Phi}\Delta\rho^{c/m}(\Omega')D_{M,0}^{k}(\Omega')\delta D_{M}(\Omega')P_{n}(t)\,d\Omega'\\&=\sum_{m=-n}^{n}(\Delta\rho\delta M)_{n,m}^{(k)}\,Y_{n,m}(\Omega).\end{aligned} \tag{9.3}$$

10. GLOBAL GRAVIMETRIC MOHO MODEL

As discussed in Chapter 9, the uniform density contrast at the Moho interface has been often assumed in gravimetric methods for the regional and global Moho recovery. Several different average values of the Moho density contrast were reported and applied in various gravimetric studies. The average value 600 kg m^{-3} (see e.g., Heiskanen and Moritz 1967) is, for instance, typically used to compute the Airy's isostatic gravity anomalies. Dziewonski and Anderson (1981) adopted the value 480 kg m^{-3} in the definition of the PREM parameters. This value was derived from the analysis of available global seismic data. Tenzer et al. (2009a) estimated the average value of the Moho density contrast based on minimizing the global spatial correlation between the mantle gravity disturbances and the Moho depths taken from the CRUST2.0 seismic crustal model (Bassin et al. 2000). According to their result, the average Moho density contrast is 520 kg m^{-3}. Later, Tenzer et al. (2012c) updated this value to 485 kg m^{-3} based on using more recent datasets and more accurate numerical models. Sjöberg and Bagherbandi (2011) estimated the global average of the Moho density contrast based on solving the VMM isostatic model. They reported the value 448±187 kg m^{-3}.

In the most recent study, Tenzer et al. (2015f) estimated the average value of the Moho density contrast based on minimizing a spatial correlation between the mantle gravity disturbances and the CRUST1.0 Moho geometry. Their results revealed that the minimum correlation was attained for the Moho density contrast 445 kg m^{-3}. This value very closely agrees with the global average 448 kg m^{-3} estimated by Sjöberg and Bagherbandi (2011), but differs about 7% from the value 485 kg m^{-3} reported by Tenzer et al. (2012c) and from the PREM value 480 kg m^{-3} (cf. Dziewonski and Anderson 1981).

The results of seismic and gravimetric studies revealed that the Moho density contrast varies significantly. Goodacre (1972), for instance, reported the continental Moho density contrast 200 kg m^{3} in Canada. Martinec (1994) claimed that the value 600 kg m^{-3} agrees better with the Moho density contrast under the oceanic crust. He also estimated the average value 280 kg m^{-3} under the continental crust by minimizing the external gravitational potential induced by the Earth's topographic masses and the Moho discontinuity by assuming that the Moho density contrast is constant. Niu and James (2002) and Jordi (2007) determined the Moho density contrast

regionally from seismic studies using the wave-receiver functions. Their results indicate that the density contrast regionally varies as much as from 160 kg m^3 (for the mafic lower crust) to 440 kg m^{-3} (for the felsic lower crust), with an apparently typical value 440 kg m^{-3} for the craton. Sjöberg and Bagherbandi (2011) estimated that the Moho density contrast varies globally from 81.5 kg m^{-3} (in the Pacific region) to 988 kg m^{-3} (beneath the Tibetan Plateau). Furthermore, they provided the average values 678±78 kg m^{-3} and 334±108 kg m^{-3} for the continental and oceanic areas respectively. Tenzer et al. (2013) reported a similar range of the Moho density contrast (taken relative to the reference crustal density 2670 kg m^{-3}) between 82 and 965 kg m^{-3}, with a mean 441 kg m^{-3}. They also demonstrated that the Moho density contrast under the oceanic crust is highly spatially correlated with age of the the oceanic lithosphere. Tenzer and Bagherbandi (2013) investigated the structure of the Moho density contrast beneath the Antarctic crust. They reported large values of the Moho density contrast in the central part of East Antarctica and the Transantarctic mountain range, with values there typically exceeding 500 kg m^{-3}, and maxima up to 682 kg m^{-3}. According to their result, the Moho density contrast in West Antarctica is typically between 400 and 500 kg m^{-3} (apart from local maxima up to about 550 kg m^{-3} in the central Antarctic Peninsula). They also explained the local minima (400-450 kg m^{-3}) beneath the West-Antarctic rift zone and Ross Embayment by volcanic compositions along this divergent tectonic zone. These large Moho density contrast variations indicate that the assumption of a uniform model might not be sufficient for an accurate determination of the Moho geometry from gravity data, especially in global studies and in areas with a complex lithospheric structure. A possible method of dealing with this problem was proposed by Sjöberg and Bagherbandi (2011) based on a simultaneous estimation of the Moho depth and density contrast. An alternative approach was applied by Tenzer et al. (2015f) by incorporating the variable Moho density contrast as the *a priori* information in the gravimetric determination of the Moho depth (Chapter 9). This method is applied in this chapter to determine globally the Moho depth.

The mantle gravity disturbances were obtained from the consolidated crust-stripped gravity disturbances after removing the gravitational signature of the Moho geometry. The resulting gravity disturbances comprise mainly the gravitational signal of density heterogeneities within the mantle lithosphere

and the sub-lithospheric mantle (i.e., the asthenosphere). However, these gravity data still comprise some redundant gravitational signal of crustal structures and possibly also from the Moho geometry due to the ESCM180 and CRUST1.0 model uncertainties. The gravitational signature of the sub-crustal lithospheric structure is evident, for instance, over oceans (Fig. 10.1). The gravity minima are along the mid-oceanic ridges and hotspots, and the corresponding gravity maxima are along the oceanic subduction zones. As demonstrated in Chapter 8, these features are attributed to a thermal state of the oceanic lithosphere (Tenzer et al. 2015d). The gravity minima over land coincide with the divergent tectonic plate boundaries, and distinctively mark the continental rift zones (e.g., the West-Antarctic, East-African, and Baikal rift zones). In contrast, the gravity maxima are seen mainly over significant orogens. The mantle gravity disturbances are everywhere positive. This is explained by the presence of a systematic bias due to unmodelled mantle density heterogeneities. This systematic bias propagates into the gravimetric Moho solution. The mantle gravity disturbances were used to determine the Moho depths according to Eq. (9.1). The result is shown in Fig. 10.2.

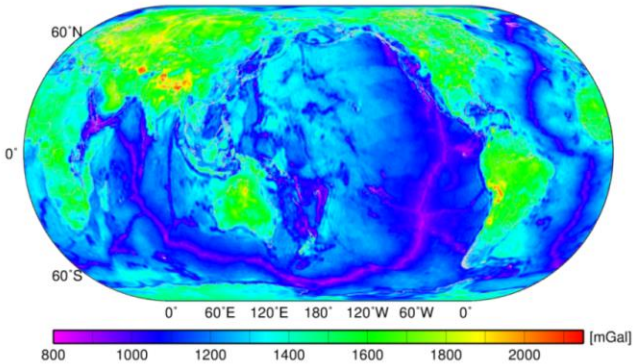

Fig. 10.1 *Mantle gravity disturbances (mGal).*

Table 10.1 *Statistics of the CRUST1.0* $D_{\mathrm{CRUST1.0}}$ *and gravimetric* $D_{\Delta\rho}$ *Moho depths.*

Moho depths	**Min** [km]	**Max** [km]	**Mean** [km]	**STD** [km]
$D_{\Delta\rho}$	0.9	71.8	13.2	12.4
$D_{\mathrm{CRUST1.0}}$	7.4	74.8	22.9	12.4

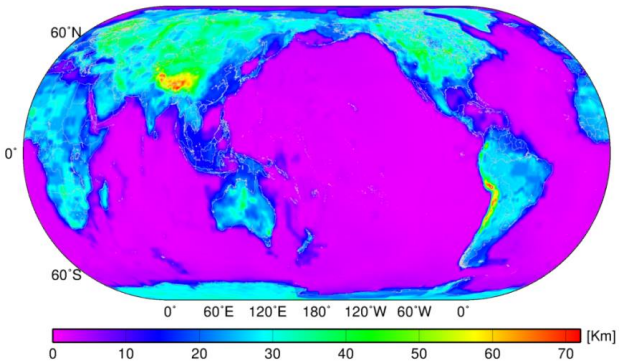

Fig. 10.2 *Gravimetric Moho depth solution (km).*

The gravimetric Moho solution exhibited a typical pattern of the Moho geometry, with an enhanced contrast between the thick continental and thinner oceanic crust. The Moho depth maxima were confirmed under orogens of Andes, Himalayas, and Tibet. The validation of the gravimetric Moho solution with CRUST1.0 seismic Moho model revealed that gravimetric solution is systematically biased about 9.7 km relative to CRUST1.0 (cf. Table 10.1). This systematic bias is explained by the gravitational signal of unmodelled deep mantle density heterogeneities. On the other hand, the gravimetric solution has a relatively good agreement with CRUST1.0 in terms of the RMS of their differences of only 3.0 km.

11. SUB-CRUSTAL STRESS FIELD

To investigate the sub-crustal stress induced by the mantle convection, Runcorn (1964, 1967) formulated its functional relation with the gravity field. He simplified the Navier-Stokes' equations to derive the horizontal components of the sub-crustal stress based by assuming a two-layered Earth's model. He then used low-degree spherical harmonics of the Earth's gravity field to deduce the global horizontal stress pattern, and found a correlation between the convergent and divergent sites established by the plate theory. The sub-crustal stress is generated mainly by the mantle convection, active tectonics, crustal and mantle density heterogeneities, crustal load of

isostatically uncompensated topographic features and mass density heterogeneities, crustal flexure, and thermal stresses (see Zoback and Zoback 1980). The sub-crustal stress has been studied also in context of interpreting the mantle convection, tectonic and magnetic features, deep earthquake mechanisms, volcanism, subduction, heat flow, kimberlite magmatism, and ore concentration (cf. Liu 1977, 1978, 1979). Eshagh and Tenzer (2015) argued that the Runcorn's definition has a limited spectral resolution only up to degree 25 of spherical harmonics due to the divergence of an asymptotically-convergent series above this degree. Moreover, Runcorn (1964) assumed only a constant value of the Moho depth. To overcome these theoretical deficiencies, Eshagh and Tenzer (2015) proposed a procedure based on utilizing the stress function with a subsequent numerical differentiation in order to improve the spectral resolution of the sub-crustal stress. They demonstrated that a series expansion of the stress function is convergent (at least) up to degree 180. They also incorporated the VMM isostatic model (Sjöberg 2009) in definition of the stress function. The stress field is then computed for a variable Moho geometry instead of assuming only a constant Moho depth (Runcorn 1964). Eshagh and Tenzer (2015) derived the stress function S in the following form

$$S = \frac{\mathrm{g}\,\Delta\rho^{\mathrm{c/m}}}{s^2}\sum_{n=2}^{\bar{n}}\frac{1}{(n-1)s^{n+1}}\left[\frac{2n+1}{n+1}\frac{\left(\bar{\rho}^{\mathrm{c}}\mathrm{H}\right)_{\mathrm{n}}}{2\Delta\rho^{\mathrm{c/m}}}-\mathrm{M}_{\mathrm{n}}\right], \tag{11.1}$$

where g is the mean gravity at the Earth's surface, $\Delta\rho^{\mathrm{c/m}}$ is a constant value of the Moho density contrast, the argument $s=1-D_M/R$ is a function of the Moho depth D_M, M_{n} denote the Moho-depth spherical functions, and $\left(\bar{\rho}^{\mathrm{c}}\,\mathrm{H}\right)_{\mathrm{n}}$ are the spherical harmonics of the solid topography (scaled by a crustal density distribution function). The Moho-depth spherical functions M_{n} are determined according to Sjöberg (2009) by solving the VMM inverse problem of isostasy. The computation of the horizontal coordinate components $S_x\mathbf{e}_{\theta}$ and $S_y\mathbf{e}_{\lambda}$ from the stress function S is then realized by applying the numerical differentiation. This method allows computing the horizontal sub-crustal stress components with a spectral resolution compatible with the global crustal models currently available. In contrast, the Runcorn's (1967) formula has a limited spatial resolution up to degree 25 due

to the divergence of an asymptotically-convergent series. This improvement was achieved by applying the stress function which is defined based on using the Laplace harmonics, instead of their partial derivatives. The convergence domain of these two methods is demonstrated in Fig. 11.1.

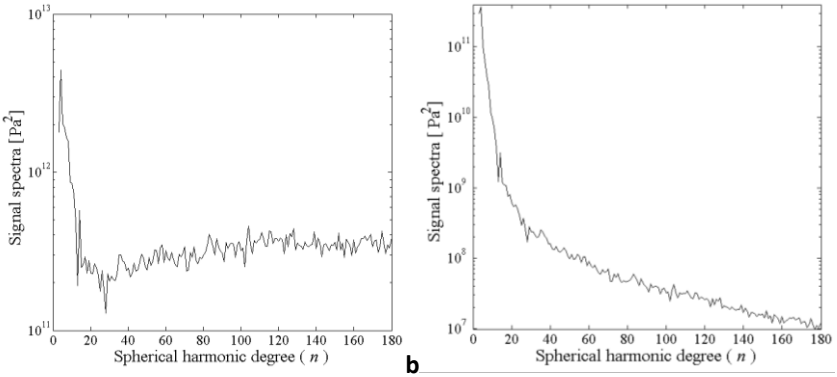

Fig. 11.1 *Power spectra of the globally-averaged: (**a**) sub-crustal stress components* $\overline{S}_H$ *(i.e., the Runcorn's method), and (**b**) the stress function* $\overline{S}$.

12. TERRESTRIAL SUB-CRUSTAL STRES FIELD

Eshagh and Tenzer (2015) applied the method reviewed in Chapter 11 to investigate a global pattern of the terrestrial sub-crustal stress field and its relation with the global tectonic configuration. This method was also applied to investigate the regional stress field. Tenzer and Eshagh (2015) studied the distribution and tectonic characteristics of the sub-crustal stress in the Taiwan region. Tenzer et al. (2015c) studied the stress field under major orogens in the central Eurasia.

The global map of the sub-crustal stress intensity is shown in Fig. 12.1, and the regional study in the central Eurasia is shown in Fig. 12.2. As seen in Fig. 12.1, the sub-crustal stress distribution closely resembles the global tectonic configuration. Most of the stress intensity is accumulated along tectonic plate boundaries. The (sub-crustal) intra-plate stress field is, on the other hand, much less pronounced or almost completely absent, except for some more localized features. Locations of the intra-plate stress anomalies typically coincide with the hotspots (i.e., Hawaii, Reunion, Mauritius) and the intra-plate tectonic features. It is worth mentioning here that the Island hotspot is

located directly at the tectonic margin, while the Hawaii, Reunion, and Mauritius hotspots have intra-plate locations. The tectonic signature in the stress field is superposed over a weaker (long-wavelength) signal of the thermal and compositional mantle structure. Moreover, the signature of the postglacial rebound in Hudson Bay, Fennoscandia, and Antarctica in the stress field is not clearly recognized.

The stress field along tectonic margins is mainly concentrated along the convergent tectonic plate boundaries. Maxima of the sub-crustal stress distinctively mark the oceanic subduction zones as well as the tectonically active continent-to-continent collision zones. In contrast, the divergent tectonic plate boundaries along the mid-oceanic ridges and the continental rift zones (i.e., the East-African, West-Antarctic, and Baikal rift zones) are without the presence of the sub-crustal stress. The largest stress intensity, detected along the oceanic subduction zones (Kurile, Japan, Mariana, Philippine, Bougainville, Tonga, and Kermadec trenches in the west Pacific; Cascadia, Peru-Chile, and Central America trenches in the East Pacific; Aleutian trench in the north Pacific; Puerto-Rico and South Sandwich trenches in the Atlantic Ocean; and Java trench in the Indian Ocean), is likely explained by a shear stress due to the subduction of the oceanic lithosphere underneath either the oceanic or continental plates. Large stress anomalies along the (continent-to-continent) collision of the African and Indian plates with the Eurasian plate observed along the Himalayan, Alpine, and Anatolian orogenic formations are again likely attributed to a shear stress due to the subduction.

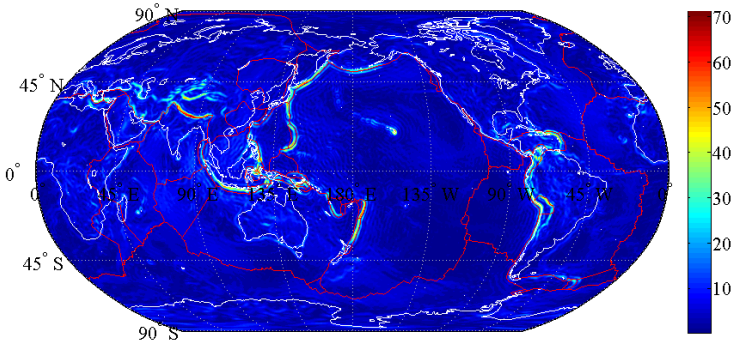

Fig. 12.1 *Global map of the sub-crustal stress intensity (MPa). Red lines show tectonic plate boundaries.*

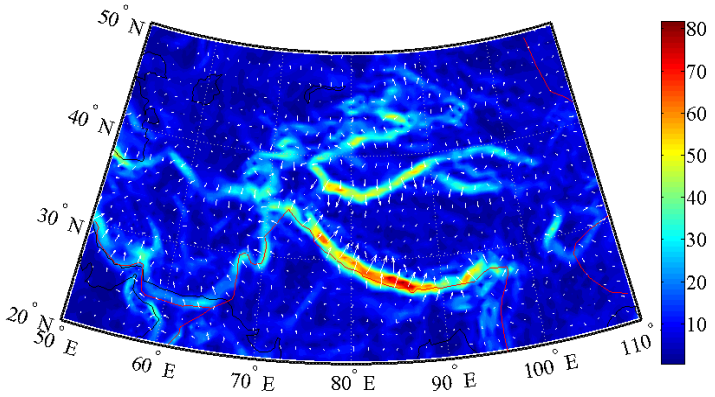

Fig. 12.2 *Regional map of the sub-crustal stress vectors and their intensity (MPa) in the central Eurasia.*

As seen from these results, most of the sub-crustal stresses occur along the inter-plate tectonic boundaries, while the intra-plate tectonic stress is much less pronounced. The largest stress anomalies were detected along the seismically active convergent tectonic plate boundaries, with the maximum intensity generated by the oceanic subduction. The oceanic subduction generates a shear stress along the convergent plate boundaries with possibly additional tensional stresses attributed to a back-arc rifting. A shear stress is also generated by the continent-to-continent plate collision. The stress intensity attenuates along transform zones, and diminishes along divergent sections. As seen in Fig. 12.2, the convergent pattern of stress vectors agrees with the compressional tectonism of orogenic formations, while their divergent orientation indicates the existence of the extensional tectonism of continental basins. A spatial distribution of the stress anomalies at the hotspots, characterized by the pronounced stress intensity around volcanic arcs (including seamounts) and absent directly at the hotspot locations, was explained by a crustal load of volcanic accumulations which are not fully isostatically compensated.

13. MARTIAN SUB-CRUSTAL STRESS FIELD

The findings in Chapter 12 support the concept that most of the terrestrial sub-crustal stresses are related to the active global tectonism. This, however,

might not be the case for other planetary bodies in the solar system due to their different geological origin and evolution. Recent studies, for instance, revealed that tectonic features on the Martian surface have a regional character, while there is no evidence of the active global tectonism in a more recent geological history of Mars (e.g., Zuber 2001). To address these issues, Tenzer at al. (2015a) investigated a possible presence of the global tectonic signature in the Martian sub-crustal stress field.

Tenzer at al. (2015a) used the Mars Orbiter Laser Altimeter (MOLA) topographic data and the MRO110B2 Martian gravity model to determine the Martian crustal thickness with a spectral resolution complete to a spherical harmonic degree 85. The VMM Moho depths were determined for the uniform Moho density contrast 600 kg m^{-3} (Neumann et al. 2004). This density contrast is representative for the olivine upper-mantle density 3500 kg m^{-3}, derived based on geochemical analysis of the sergottite, nakhlite, and chassigny (SNC) class of meteorites (Sohl and Spohn 1997). It is worth mentioning that some geochemical models imply pyroxene as a major mineral in the olivine-pyroxene-garnet chemical composition of the Martian upper mantle. The Martian crustal thickness is shown in Fig. 13.1. This Moho model was then used to determine the Martian sub-crustal stress field. The result is shown in Fig. 13.2.

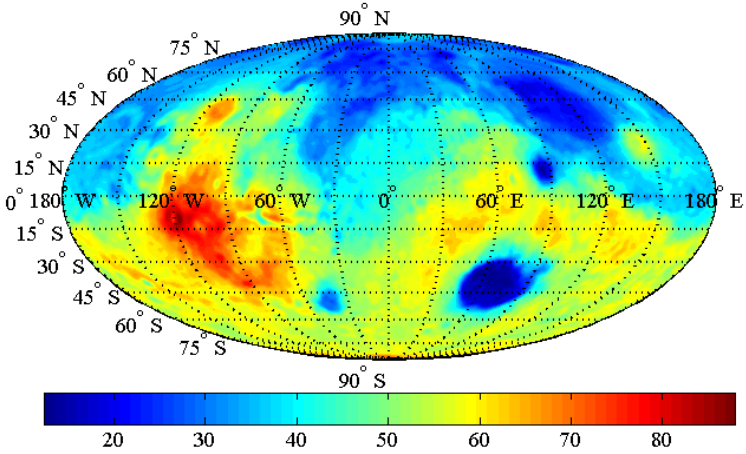

Fig. 13.1 *Martian crustal thickness (km).*

The Martian crustal thickness varies between 12.3 and 89.5 km (see Fig. 13.1). This range (77.2 km) is about 20% smaller than the crustal thickness variations (96.2 km) found by Neumann et al. (2004). Compared to their crustal model, the VMM Moho solution presented by Tenzer at al. (2015a) underestimated the crustal thickness in the Tharsis province, while overestimated the crustal thickness under major impact basins. These differences are due to applying the VMM isostatic model based on a global compensation principle that better represents the reality than the Airy's local compensation scheme assumed in previous studies. Neumann et al. (2004), however, modeled more accurately the actual crustal structures by using different density values for specific geological formations on Mars. According to Tenzer at al. (2015a), the average Martian crustal thickness is 46.4 km. This average value is within the interval of previous estimates reported by Zuber et al. (2000), Neumann et al. (2004), and Wieczorek and Zuber (2004).

The most prominent feature in the crustal geometry is a significant contrast between a thicker crust underlying the southern highlands and a thinner crust under the northern lowlands. The crustal thickness of the northern lowlands is typically less than 40 km. The crustal thickness under most of the heavily cratered southern highlands exceeds 45 km, except for much thinner crust under Hellas and Argyre basins, with the crustal thickness decreasing to less than 30 km under Argyre basin and as low as 13 km under Hellas basin. Similarly, Utopia and Isidis basins on the northern hemisphere are characterized by a very thin crust, with the thickness locally decreasing to 20 and 14 km respectively. This significant crustal thinning is explained by a Moho uplift after impact (Neumann et al. 1996), followed by a modification due to the volcanic and sedimentary surface loads (Buczkowski and Cooke 2004). This is most prominent in Utopia basin with thick sedimentary deposits and lava covers. The crustal thickness in the Tharsis province typically exceeds 70 km. This large crustal thickness is attributed to a crustal flexure due to a load of volcanic accumulations, which is manifested by a Moho deepening extending under a broader area of the Tharsis province. The crust under the broad Arabia is thickening more gradually. In Arabia and Elysium regions the dichotomy boundary is compensated by a crustal thickness variation, with a more pronounced relief along the Moho than at the surface.

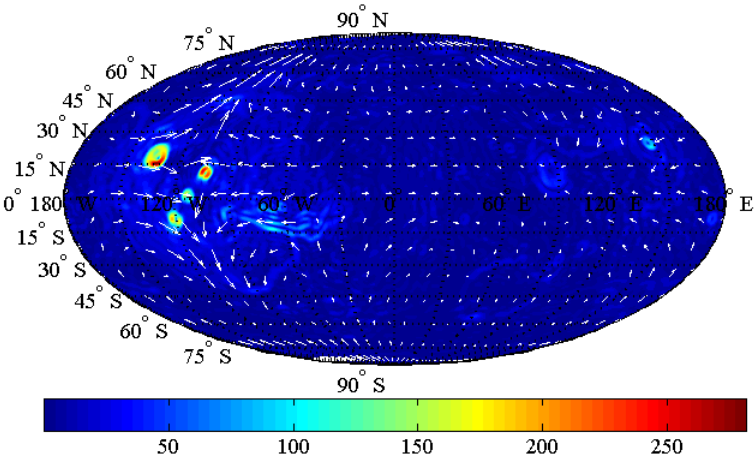

Fig. 13.2 *Martian sub-crustal stress vectors and their intensity (MPa).*

The Martian sub-crustal stress is attributed mainly to the crustal load of volcanic accumulations, the regional tectonism, and the impact of meteorites. The crustal load of Tharsis volcanic formations is likely also responsible for a regional tectonism of Valles Marineris. In contrast, the stress distribution around major impact basins was explained by a crustal extrusion after impact, followed by Moho uplift. The crustal loading generates the maximum intensity of the sub-crustal stress on Mars. This is evident in the most prominent signatures of crustal loads of Tharsis major volcanoes (Olympus, Ascraeus, Arsia, and Pavonis Mons) and that of Elysium Mons. These shield volcanoes are thus not fully isostatically compensated, the interpretation which agrees with the finding of Arkani-Hamed and Riendler (2002). In addition to these localized stress anomalies, the crustal load of Tharsis volcanic accumulations generates a large-scale stress field, which distinctively marks the Tharsis dichotomy. In contrast, the signature of the hemispheric dichotomy is absent. The incomplete isostatic compensation of the Tharsis bulge might be explained by its more recent formation compared to the (fully compensated) southern highlands. This assumption agrees with a theory of the single highland formation followed by the additional construction of Tharsis by the Hellas impact proposed by Phillips et al. (2001) as well as with the mantle-plume migration theory of Roberts and Zhong (2007). Despite the fact that the

crustal load is likely responsible for most of the Martian sub-crustal stress, the signature of polar ice load is missing. A possible explanation of this finding was given by Neumann et al. (2004). They suggested that the polar ice caps on Mars are geologically relatively young, while the isostatic adjustment to a changing load takes place over time scales at 10^5 to 10^7 years (Johnson et al. 2000). Geomorphological features of Valles Marineris and its specific stress distribution (characterized by sections of the tensional and compressional stress field) are likely explained by a regional tectonism, which is related to a crustal load of the Tharsis Bulge. This is in agreement with more recent theories of the Valles Marineris formation attributed to either a tensional fracturing (Tanaka and Golombek 1989) or a regional extensional tectonism (Banerdt et al. 1992). A better understanding of the processes which formed Valles Marineris is, however, still open to investigation.

The stress distribution on Mars and its possible origin are quite different from those observed on Earth. Tenzer and Eshagh (2015) and Eshagh and Tenzer (2015) demonstrated that most of the sub-crustal stress on Earth is generated by the active global tectonism. They also identified the additional, but much localized stress anomalies caused by a crustal loading of volcanic accumulations in vicinity of the hotspots. On Mars, the situation is opposite. Except for the regional tectonism of Valles Marineris, the tectonic signature is absent. The Martian lithosphere was thus not fractured by tectonic forces into individual plates. This finding supports a theory of the single lithospheric plate on Mars (which rotated due to a polar wander) proposed by Zhong (2009) and Sramek and Zhong (2010). Moreover, most of the Martian sub-crustal stress is generated by a crustal load of volcanic accumulations, which is likely also responsible for a regional tectonism along Valleys Marineris. Another significant difference between the stress fields of these two planets is the signature of impacts on Mars and its absence on Earth.

PUBLICATIONS THAT FORM THE BASIS OF THE THESIS

Bagherbandi M, Tenzer R (2013) Comparative analysis of Vening Meinesz-Moritz isostatic models using the constant and variable crust-mantle density contrast – a case study of Zealandia. Journal of Earth System Science 122(2): 339-348 (IF: 1.04)

Bagherbandi M, Tenzer R, Sjöberg LE, Novák P (2013) Improved global crustal thickness modeling based on the VMM isostatic model and non-isostatic gravity correction. Journal of Geodynamics 66: 25-37 (IF: 2.217)

Bagherbandi M, Tenzer R, Abrehdary M, Sjöberg LE (2015) A New Fennoscandian crustal thickness model based on CRUST1.0 and gravimetric isostatic approach. Earth-Science Review 145: 132-145 (IF: 7.885)

Chen W, Tenzer R, Gu X (2014) Sediment stripping correction to marine gravity data. Marine Geodesy 37(4): 419-439 (IF: 1.306)

Chen W, Tenzer R (2015) Harmonic coefficients of the Earth's Spectral Crustal Model 180 - ESCM180. Earth Science Informatics 8(1): 147-159 (IF: 0.743)

Eshagh M, Tenzer R (2015) Sub-crustal stress determined using gravity and crust structure models. Computational Geosciences 19(1): 115-125 (IF: 1.868)

Gladkikh V, Tenzer R (2011) A mathematical model of the global ocean saltwater density distribution. Pure and Applied Geophysics 169(1-2): 249-257 (IF: 1.618)

Gu X, Tenzer R, Gladkikh V (2014) Empirical models of the ocean-sediment and marine sediment-bedrock density contrasts. Geosciences Journal 18(4): 439-447 (IF: 0.917)

Novak P, Tenzer R, Eshagh M, Bagherbandi M (2013) Evaluation of gravitational gradients by Earth's crustal structures. Computer and Geosciences 51: 22-33 (IF: 2.054)

Tenzer R, Hamayun, Vajda P (2009a) Global maps of the CRUST2.0 components stripped gravity disturbances, Journal of Geophysical Research (Solid Earth) 114: B05408 (IF: 3.426)

Tenzer R, Hamayun, Vajda P (2009b) A global correlation of the step-wise consolidated crust-stripped gravity field quantities with the topography, bathymetry, and the CRUST2.0 Moho boundary. Contributions to Geophysics and Geodesy 39(2): 133-147

Tenzer R, Vajda P, Hamayun (2009c) Global atmospheric corrections to the gravity field quantities. Contributions to Geophysics and Geodesy 39(3): 221-236

Tenzer R, Vajda P, Hamayun (2010a) A mathematical model of the bathymetry-generated external gravitational field. Contributions to Geophysics and Geodesy 40(1): 31-44

Tenzer R, Abdalla A, Vajda P, Hamayun (2010b) The spherical harmonic representation of the gravitational field quantities generated by the ice density contrast. Contributions to Geophysics and Geodesy 40(3): 207-223

Tenzer R, Novák P, Gladkikh V (2011a) On the accuracy of the bathymetry-generated gravitational field quantities for a depth-dependent seawater density distribution. Studia Geophysica et Geodaetica 55(4): 609-626 (IF: 0.806)

Tenzer R, Novák P (2012) Bathymetric stripping corrections to gravity gradient components. Earth, Planets and Space 64(7): e21-e24 (IF: 1.328)

Tenzer R, Bagherbandi M (2012) Reformulation of the Vening-Meinesz Moritz inverse problem of isostasy for isostatic gravity disturbances. International Journal of Geosciences 3(5): 918-929

Tenzer R, Novák P, Gladkikh V (2012a) The bathymetric stripping corrections to gravity field quantities for a depth-dependant model of the seawater density. Marine Geodesy 35: 198-220 (IF: 1.306)

Tenzer R, Novák P, Vajda P, Gladkikh V, Hamayun (2012b) Spectral harmonic analysis and synthesis of Earth's crust gravity field. Computational Geosciences 16(1): 193-207 (IF: 1.868)

Tenzer R, Hamayun, Novák P, Gladkikh V, Vajda P (2012c) Global crust-mantle density contrast estimated from EGM2008, DTM2008, CRUST2.0, and ICE-5G. Pure and Applied Geophysics 169(9): 1663-1678 (IF: 1.618)

Tenzer R, Novák P, Hamayun, Vajda P (2012d) Spectral expressions for modelling the gravitational field of the Earth's crust density structure. Studia Geophysica et Geodaetica 56(1): 141-152 (IF: 0.806)

Tenzer R, Gladkikh V, Vajda P, Novák P (2012e) Spatial and spectral analysis of refined gravity data for modelling the crust-mantle interface and mantle-lithosphere structure. Surveys in Geophysics 33(5): 817-839 (IF: 3.447)

Tenzer R, Bagherbandi M, Gladkikh V (2012f) Signature of the upper mantle density structure in the refined gravity data. Computational Geosciences 16(4): 975-986 (IF: 1.868)

Tenzer R, Bagherbandi M, Vajda P (2013) Global model of the upper mantle lateral density structure based on combining seismic and isostatic models. Geosciences Journal 17(1): 65-73 (IF: 0.917)

Tenzer R (2013a) Inverse problem for the gravimetric modeling of the crust-mantle density contrast. Contributions to Geophysics and Geodesy 43(2): 83-98

Tenzer R (2013b) Inverse problem for the gravimetric modeling of the crust-mantle density contrast. Contributions to Geophysics and Geodesy 43(2): 83-98

Tenzer R, Bagherbandi M (2013) Reference crust-mantle density contrast beneath Antarctica based on the Vening Meinesz-Moritz isostatic problem and CRUST2.0 seismic model. Earth Sciences Research Journal 17(1): 7-12 (IF: 0.243)

Tenzer R, Gladkikh V (2014) Assessment of density variations of marine sediments with ocean and sediment depths. The Scientific World Journal, ID 823296, p 9

Tenzer R, Chen W (2014a) Expressions for the global gravimetric Moho modeling in spectral domain. Pure and Applied Geophysics 171(8): 1877-1896 (IF: 1.618)

Tenzer R, Chen W (2014b) Regional gravity inversion of crustal thickness beneath the Tibetan plateau. Earth Science Informatics 7: 265-276 (IF: 0.743)

Tenzer R (2015) Mathematical models of the Earth's density structure and their applications in gravimetric forward modeling. Contributions to Geophysics and Geodesy 45(2): 67-92

Tenzer R, Eshagh M (2015) Sub-crustal stress in the Taiwan region. Terrestrial, Atmospheric and Oceanic Sciences 26(3): 261-268 (IF: 0.703)

Tenzer R, Eshagh M, Jin S (2015a) Martian sub-crustal stress from gravity and topographic models. Earth and Planetary Science Letters 425: 84-92 (IF: 4.734)

Tenzer R, Chen W, Ye Z (2015b) Empirical model of the gravitational field generated by the oceanic lithosphere. Advances in Space Research 55(1): 72-82 (IF: 1.358)

Tenzer R, Eshagh M, Shen W (2015c, submitted) Distribution of the sub-crustal stress in central Eurasia. Geosciences Journal (IF: 0.917)

Tenzer R, Chen W, Ye Z (2015d) Empirical model of the gravitational field generated by the oceanic lithosphere. Advances in Space Research 55(1): 72-82 (IF: 1.358)

Tenzer R, Chen W, Tsoulis D, Bagherbandi M, Sjöberg LE, Novák P, Jin S (2015e) Analysis of the refined CRUST1.0 crustal model and its gravity field. Surveys in Geophysics 36(1): 139-165 (IF: 3.447)

Tenzer R, Chen W, Jin S (2015f) Effect of the upper mantle density structure on the Moho geometry. Pure and Applied Geophysics 172(6): 1563-1583 (IF: 1.618)

Vajda P, Vaníček P, Novák P, Tenzer R, Ellmann A (2007) Secondary indirect effects in gravity anomaly data inversion or interpretation. Journal of Geophysical Research - Solid Earth 112: B06411 (IF: 3.426)

Note that all impact factors (IF) were retreived from: http://www.medsciediting.com/sci/ (Date: 01/12/2015)

REFERENCES

Airy GB (1855) On the computations of the effect of the attraction of the mountain masses as disturbing the apparent astronomical latitude of stations in geodetic surveys. Translations of Royal Society, London, Series B, Vol 145

Amante C, Eakins BW (2009) ETOPO1 1 Arc-minute global relief model: Procedures, data sources and analysis, NOAA, Technical Memorandum, NESDIS, NGDC-24, pp 19

Arabelos D, Mantzios G, Tsoulis D (2007) Moho depths in the Indian Ocean based on the inversion of satellite gravity data. Advances in Geosciences, Vol. 9: Solid Earth, Ocean Science and Atmospheric Science, (Eds) Huen W, Chen YT, World Scientific Publishing, pp 41-52

Arkani-Hamed J, Riendler L (2002) Stress differences in the Martian lithosphere: Constrains on the thermal state of Mars. Journal of Geophysical Research 107(E12): 5119

Bagherbandi M, Eshagh M (2011) Recovery of Moho's undulations based on the Vening Meinesz-Moritz theory from satellite gravity gradiometry data: A simulation study, Advances in Space Research 49(6): 1097-1111

Bagherbandi M, Eshagh M (2012) Crustal thickness recovery using an isostatic model and GOCE data, Earth, Planets and Space 64(11): 1053-1057

Bagherbandi M, Sjöberg LE (2012b) Non-isostatic effects on crustal thickness: A study using CRUST2.0 in Fennoscandia. Physic of Earth and Planetary Interiors 200-201: 37-44

Banerdt WB, Golombek MP, Tanaka KL (1992) Stress and tectonics on Mars. In: Mars, Kieffer HH, Jakosky BM, Snyder CW, Matthews MS (Eds), University of Arizona Press, Tucson, AZ, pp 249-297

Bassin C, Laske G, Masters G (2000) The current limits of resolution for surface wave tomography in North America. EOS, Trans AGU, 81, F897

Bowin C, Scheer E, Smith W (1986) Depth estimates from ratio of gravity, geoid and gravity gradient anomalies. Geophysics 51(1): 123-136

Braitenberg C, Zadro M (1999) Iterative 3D gravity inversion with integration of seismologic data. Bolletino Geofysica Teoretica Applicata 40(3-4): 469-476

Braitenberg C, Mariani P, Reguzzoni M, Ussami N (2010) GOCE observations for detecting unknown tectonic features. In: Proc. of the ESA Living Planet Symposium, 28 June - 2, July 2010, Bergen, Norway, ESA, SP-686

Buczkowski DL, Cooke ML (2004) Formation of double-ring circular grabens due to volumetric compaction over buried impact craters: Implications for thickness and nature of cover material in Utopia Planitia, Mars, Journal of Geophysical Research 109(E2): E02006

Carlson RL, Raskin GS (1984) Density of the ocean crust. Nature 311: 555-558

Cowie PA, Karner GD (1990) Gravity effect of sediment compaction: examples from the North Sea and the Rhine Graben. Earth and Planetary Science Letters 99: 141-153

Christensen NI, Mooney WD (1995) Seismic velocity structure and composition of the continental crust: a global view. Journal of Geophysical Research 100(B7): 9761-9788

Čadek O, Martinec Z (1991) Spherical harmonic expansion of the earth's crustal thickness up to degree and order 30. Studia Geophysica et Geodaetica 35: 151-165

Dziewonski AM, Anderson DL (1981) Preliminary Reference Earth Model. Physic of Earth and Planetary Interiors 25: 297-356

Eckhardt DH (1983) The gains of small circular, square and rectangular filters for surface waves on a sphere. Bulletin Géodésique 57: 394-409

Ekholm S (1996) A full coverage, high-resolution, topographic model of Greenland, computed from a variety of digital elevation data. Journal of Geophysical Research B10, 21: 961–972

Eshagh M, Bagherbandi M, Sjöberg LE (2011) A combined global Moho model based on seismic and gravimetric data. Acta Geodaetica et Geophysica Hungarica 46(1): 25-38

Garrison T (2001) Essentials of oceanography, Pacific Grove, CA, Brooks Cole

Geiss E (1987) A new compilation of crustal thickness data for the Mediterranean area. Annals of Geophysics 5B: 623-630

Goodacre AK (1972) Generalized structure and composition of the deep crust and upper mantle in Canada, Journal of Geophysical Research 77: 3146-3160

Hamilton EL, Menard HW (1956) Density and porosity of sea floor sediments off San Diego, California. Bulletin - American Association of Petroleum Geologists 40, p 754

Hamilton EL (1976) Variations of density and porosity with depth in deep-sea sediments. Journal of Sedimentary Petrology 46(2,1): 280-300

Heiskanen WH, Moritz H (1967) Physical geodesy. San Francisco, Freeman WH and Co

Hinze WJ (2003) Bouguer reduction density, why 2.67? Geophysics 68(5): 1559-1560

Hüneke H, Mulder T (2011) Deep-Sea sediments. Developments in sedimentology, 63, Elsevier, New York, p 849

Johnson CL, Solomon SC, Head JW, Phillips RJ, Smith DE, Zuber MT (2000) Lithospheric loading by the north polar cap of Mars. Icarus 144: 313-328

Jordi J (2007) Constraining velocity and density contrasts across the crust–mantle boundary with receiver function amplitudes, Geophysical Journal International 171: 286-301

Kaban MK, Schwintzer P, Tikhotsky SA (1999) Global isostatic gravity model of the Earth. Geophysical Journal International 136: 519-536.

Kaban MK, Schwintzer P, Artemieva IM, Mooney WD (2003) Density of the continental roots: compositional and thermal contributions, Earth and Planetary Science Letters 209: 53-69

Kaban MK, Schwintzer P, Reigber Ch (2004) A new isostatic model of the lithosphere and gravity field. Journal of Geodesy 78: 368-385

Laske G, Masters G (1997) A global digital map of sediment thickness. EOS Trans, AGU 78: F483

Laske G, Masters G, Ma Z, Pasyanos ME (2012) CRUST1.0: An updated global model of Earth's crust. Geophysical Research Abstracts 14, EGU2012-3743-1, EGU General Assembly 2012

Liu HS (1977) Convection pattern and stress system under the African plate. Physics of Earth and Planetary Interiors 15: 60-68

Liu HS (1978) Mantle convection pattern and subcrustal stress under Asia. Physics of Earth and Planetary Interiors 16: 247-256

Liu HS (1979) Convection-generated stress concentration and seismogenic models of the Tangshan Earthquake. Physics of Earth and Planetary Interiors 19: 307-318

Lythe MB, Vaughan DG, BEDMAP consortium (2001) BEDMAP, a new ice thickness and subglacial topographic model of Antarctica. Journal of Geophysical Research, B, Solid Earth Planets 106(6): 11335-11351

Mayer-Guerr T, Rieser D, Höck E, Brockmann JM, Schuh W-D, Krasbutter I, Kusche J, Maier A, Krauss S, Hausleitner W, Baur O, Jäggi A, Meyer U, Prange L, Pail R, Fecher T, Gruber T (2012) The new combined satellite only model GOCO03s: Abstract, GGHS2012, Venice

Martinec Z (1994) The density contrast at the Mohorovičič discontinuity, Geophysical Journal International 117: 539-544

Millero FJ, Feistel R, Wright DG, McDougall TJ (2008) Deep Sea Research Part I, Oceanographic Research Papers 55(1): 50-72

Moritz H (1990) The figure of the Earth. Wichmann H, Karlsruhe, p 279

Moritz H (2000) Geodetic Reference System 1980. Journal of Geodesy 74: 128162

Neumann GA, Zuber MT, Smith DE, Lemoine FG (1996) The lunar crust: Global structure and signature of major basins, Journal of Geophysical Research 101: 16841-16863

Neumann GA, Zuber MT, Wieczorek MA, McGovern PJ, Lemoine FG, Smith DE (2004) Crustal structure of Mars from gravity and topography. Journal of Geophysical Research 109: E08002

Niu F, James DE (2002) Fine structure of the lowermost crust beneath the Kaapvaal craton and its implications for crustal formation and evolution. Earth and Planetary Science Letters 200: 121-130

Oldenburg DW (1974) The inversion and interpretation of gravity anomalies. Geophysics 39: 526-536

Parsons B, Sclater JG (1977) An analysis of the variation of ocean floor bathymetry and heat flow with age. Journal of Geophysical Research 82(5): 803-827

Phillips RJ, Zuber MT, Solomon SC, Golombek MP, Jakosky BM, Banerdt WB, Smith DE, Williams RME, Hynek BM, Aharonson O, Hauck SA (2001) Ancient geodynamics and global-scale hydrology on Mars. Science 291: 2587-2591

Pratt JH (1855) On the attraction of the Himalaya Mountains and of the elevated regions beyond upon the plumb-line in India. Translations of Royal Society London, B, 145

Roberts JH, Zhong S (2007) The cause for the north-south orientation of the crustal dichotomy and the equatorial location of Tharsis on Mars. Icarus 190: 24-31

Rogers N, Blake S, Burton K (2008) An introduction to our dynamic planet. Cambridge University Press

Runcorn SK (1964) Satellite gravity measurements and laminar viscous flow model of the Earth mantle. Journal of Geophysical Research 69(20): 4389-4394

Runcorn SK (1967) Flow in the mantle inferred from the low degree harmonics of the geopotential. Geophysical Journal Research of Astronomical Society 14: 375-384

Sampietro D (2011) GOCE exploitation for Moho modeling and applications. In: Proceedings of the 4th International GOCE User Workshop, 31 March - 1 April 2011, Munich, Germany

Sampietro D, Reguzzoni M, Braitenberg C (2013) The GOCE estimated Moho beneath the Tibetan Plateau and Himalaya. In: Rizos C, Willis P (Eds), International Association of Geodesy Symposia, Earth on the Edge: Science for a Sustainable Planet, Proceedings of the IAG General Assembly, 28 June - 2 July 2011, Melbourne, Australia, Vol 139, Springer-Verlag, Berlin

Sjöberg LE (2009) Solving Vening Meinesz-Moritz Inverse Problem in Isostasy. Geophysical Journal International 179: 1527-1536

Sjöberg LE (2013) On the isotactic gravity anomaly and disturbance and their applications to Vening Meinesz-Moritz gravimetric inverse problem. Geophysical Journal International 193(3): 1277-1282

Sjöberg LE, Bagherbandi M (2011) A method of estimating the Moho density contrast with a tentative application by EGM08 and CRUST2.0. Acta Geophysica 58: 1-24

Sohl F, Spohn T (1997) The interior structure of Mars: Implications from SNC meteorites. Journal of Geophysical Research 102: 1613-1635

Sramek O, Zhong S (2010) Long-wavelength stagnant lid convection with hemispheric variation in lithospheric thickness: Link between Martian crustal dichotomy and Tharsis? Journal of Geophysal Research 115: E09010

Stewart RH (2008) Introduction to Physical Oceanography. Texas AM University

Sykes TJS (1996) A correction for sediment load upon the ocean floor: Uniform versus varying sediment density estimations - implications for isostatic correction. Marine Geology 133(1-2): 35-49

Tanaka KL, Golombek MP (1989) Martian tension fractures and the formation of grabens and collapse features at Valles Marineris: Proceedings of the 19th Lunar and Planetary Science Conference, pp 383-396

Vening Meinesz FA (1931) Une nouvelle méthode pour la réduction isostatique régionale de l'intensité de la pesanteur. Bulletin Géodésique 29: 33-51

Zhong S (2009) Migration of Tharsis volcanism on Mars caused by differential rotation of the lithosphere. Nature Geosciences 2: 19-23

Zuber MT, SC Solomon, RJ Phillips, Smith DE, Tyler GL, Aharonson O, Balmino G, Banerdt WB, Head JW, Johnson CL, Lemoine FG, McGovern PJ, Neumann GA, Rowlands DD, Zhong S (2000) Internal structure and early thermal evolution of Mars from Mars Global Surveyor topography and gravity. Science 287: 1788-1793

Zuber MT (2001) The crust and mantle of Mars. Nature 412(12): 220-227

Wieczorek MA, Zuber MT (2004) The thickness of the Martian crust: Improved constraints from geoid-to-topography ratios. Journal of Geophysical Research 109(E1): E01009

Williams DL (1975) On the thermal evolution of the oceanic lithosphere. Geophysical Research Letters 2: 321-323